J. Fluid Mech. (2012), *vol.* 709, *pp.* 1–36.
doi:10.1017/jfm.2012.104

Experimental study of particle-driven secondary flow in turbulent pipe flows

R. J. Belt, A. C. L. M. Daalmans and L. M. Portela†

Multi-Scale Physics Department, J. M. Burgerscentrum for Fluid Mechanics, Delft University of Technology, Leeghwaterstraat 39, 2628 CB Delft, The Netherlands

(Received 1 July 2011; revised 9 December 2011; accepted 21 February 2012; first published online 24 August 2012)

In fully developed single-phase turbulent flow in straight pipes, it is known that mean motions can occur in the plane of the pipe cross-section, when the cross-section is non-circular, or when the wall roughness is non-uniform around the circumference of a circular pipe. This phenomenon is known as secondary flow of the second kind and is associated with the anisotropy in the Reynolds stress tensor in the pipe cross-section. In this work, we show, using careful laser Doppler anemometry experiments, that secondary flow of the second kind can also be promoted by a non-uniform non-axisymmetric particle-forcing, in a fully developed turbulent flow in a smooth circular pipe. In order to isolate the particle-forcing from other phenomena, and to prevent the occurrence of mean particle-forcing in the pipe cross-section, which could promote a different type of secondary flow (secondary flow of the first kind), we consider a simplified well-defined situation: a non-uniform distribution of particles, kept at fixed positions in the 'bottom' part of the pipe, mimicking, in a way, the particle or droplet distribution in horizontal pipe flows. Our results show that the particles modify the turbulence through 'direct' effects (associated with the wake of the particles) and 'indirect' effects (associated with the global balance of momentum and the turbulence dynamics). The resulting anisotropy in the Reynolds stress tensor is shown to promote four secondary flow cells in the pipe cross-section. We show that the secondary flow is determined by the projection of the Reynolds stress tensor onto the pipe cross-section. In particular, we show that the direction of the secondary flow is dictated by the gradients of the normal Reynolds stresses in the pipe cross-section, $\partial\tau_{rr}/\partial r$ and $\partial\tau_{\theta\theta}/\partial\theta$. Finally, a scaling law is proposed, showing that the particle-driven secondary flow scales with the root of the mean particle-forcing in the axial direction, allowing us to estimate the magnitude of the secondary flow.

Key words: multiphase and particle-laden flows, turbulent flows

1. Introduction

Even in the case of a fully developed single-phase turbulent flow in a straight pipe, it is possible to have a mean motion in the plane of the pipe cross-section, perpendicular to the mean primary flow direction (figure 1). This mean flow in the cross-section, or 'secondary flow', occurs, for example, in pipes of non-circular cross-section (Brundrett & Baines 1964; Hinze 1973; Speziale 1982; Demuren & Rodi 1984; Nagata *et al.* 2011) or in pipes of circular cross-section with a circumferential

† Email address for correspondence: L.Portela@tudelft.nl

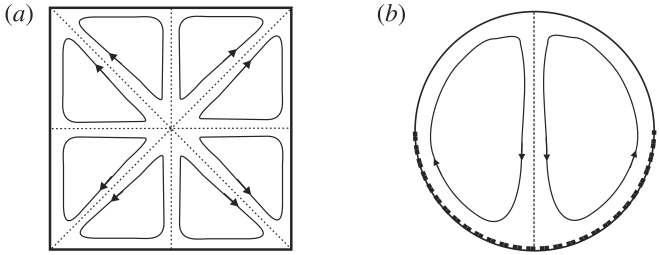

FIGURE 1. Secondary flow in the cross-section of a square pipe (*a*) and in the cross-section of a horizontal circular pipe roughened at the bottom (*b*).

variation in the wall roughness (Darling & McManus 1968; Hinze 1973; Van't Westende *et al.* 2007). Another case where secondary flow occurs is in variable-density buoyancy-driven flows in inclined pipes of circular cross-section (Hallez & Magnaudet 2009). However, in this paper we consider only constant-density flows.

In fully developed flows in straight pipes, secondary flow is driven by turbulence. It has been referred to as secondary flow of the second kind, in contrast to secondary flow of the first kind, which is promoted by pressure gradients or buoyancy forces in the pipe cross-section, as, for example, in curved pipes. Secondary flow of the second kind has been debated for a long time in the literature, because it can have a large impact on practical engineering applications (secondary flow increases the heat and mass transfer) and especially because the explanation for its occurrence is complex. It is generally admitted now that the occurrence of secondary flow of the second kind is associated with the anisotropy in the Reynolds stress tensor in the pipe cross-section (Speziale 1982). In the case of squared pipes, the anisotropy is due to the non-circular geometry, whereas in the case of circular pipes with a non-uniform roughness it is produced by the non-uniform boundary conditions. In the case of variable-density buoyancy-driven flows in inclined circular pipes, the anisotropy is generated by the shear induced by the stratification, which is along the vertical midplane and breaks the axisymmetry in the pipe.

Secondary flows occur also in two-phase flows. For example, in gas–liquid horizontal stratified pipe flow exists a secondary flow in the gas layer and in the liquid layer (Liné, Masbernat & Soualmia 1994; Nordsveen 2001). The secondary flow in the gas layer is a secondary flow of the second kind and it can be explained by the non-uniform roughness and the non-circular geometry, similarly to single-phase flow. The secondary flow in the liquid layer is, on the other hand, generated by the interaction between the waves and the mean flow in the liquid layer.

Another example, and the one that originally motivated the current work, is horizontal gas–liquid annular flow. In gas–liquid annular flow, the liquid is distributed partly as a thin film along the wall and partly as droplets in the turbulent gas core. In horizontal pipes, because of the gravity, the film is thicker and rougher in the bottom than in the top of the cross-section. Furthermore, the concentration of droplets is also higher in the bottom than in the top. This break of the axisymmetry induces a secondary flow in the gas core. The occurrence of secondary flow has been a subject of debate in the literature, because it is believed that secondary flow is one of the mechanisms which can maintain the film in the top of the cross-section against gravity. Indeed, the circumferential variation in the film thickness leads to a circumferential variation in the interface roughness, which promotes a secondary flow in the gas core with a direction such that it exerts a drag on the film from the bottom to the top of the cross-section (Flores, Crowe & Griffith 1995), as shown in figure 1(*b*). However, there exists some experimental evidence that the secondary flow reverses direction when the amount of droplets in the bottom part of the gas core becomes important (Dykhno, Williams & Hanratty 1994). A satisfactory explanation has not been provided for this observation. However, it suggests that the interaction between the droplets and the flow in the gas core may induce a secondary flow. The study of this effect in horizontal annular flow is complicated because of the interaction between the gas core and the liquid film. Therefore, in this study we focus only on particle-driven secondary flow, noting that small droplets have a behaviour similar to solid particles. This not only eliminates the complexities associated with the presence of the liquid film but, also, makes the study more general, and not just applicable to gas–liquid horizontal annular flow.

It is known that in particle-laden flows the forcing of the flow by the particles can lead to large changes in the turbulence (Li *et al.* 2001). Therefore, a non-uniform particle distribution (for example, promoted by the gravity in horizontal pipe flow) can promote a non-uniform modification of the turbulence and lead to an anisotropy in the Reynolds stresses in the cross-section. Hence, a non-uniform particle distribution can induce a secondary flow of the second kind (Belt 2007).

The modification of the turbulence by particles can be due to (i) the momentum exchange between the particles and the fluid, acting locally around the particles; (ii) the disruption in the turbulence dynamics promoted by the presence of the particles; and (iii) the global changes in the mean axial velocity and shear-stress profiles that are required to compensate for the drag of the particles (Squires & Eaton 1990; Boivin, Simonin & Squires 1998; Li *et al.* 2001). The first mechanism is a 'direct' effect, associated with the local distortion of the flow field around the particles, whereas the other two mechanisms are 'indirect' effects, associated with the global turbulence dynamics and the balance of momentum. For small particles, the local distortion of the velocity field occurs at scales smaller than the turbulence and it does not interact with the turbulence scales. However, through the forcing, the particles can promote significant 'indirect' changes in the turbulence, and, if the particles are distributed non-uniformly, an anisotropy in the Reynolds stresses in the cross-section, promoting a secondary flow.

It is noted that this mechanism is different from the explanations given for particle-driven secondary flows of the first kind. Indeed, a forcing in the pipe cross-section due to the particles can also introduce a secondary flow. This forcing can be due, for example, to gravitational and buoyancy forces, but it can also have subtle causes. For instance, using Eulerian–Lagrangian simulations, Huber & Sommerfeld (1998) showed the existence of a secondary flow due to the forcing of the particles in an uniformly rough horizontal pipe. According to Huber and Sommerfeld, the roughness leads to a larger bouncing angle of the particles, and therefore to a transfer of momentum by the particles from the axial to the wall-normal direction, which translates into a mean forcing in the pipe cross-section. Due to the non-uniform particle distribution promoted by gravity, this mean forcing is larger in the bottom than in the top of the cross-section, therefore inducing a secondary flow of the first kind. Such a secondary flow is not caused by the anisotropy in the Reynolds stresses (Huber and Sommerfeld used a $k - \epsilon$ turbulence model, which is isotropic and unable to predict a secondary flow; Speziale 1982); it is directly linked to the effect of the pipe roughness on the particle-bouncing, and, as shown by Huber and Sommerfeld, is absent in the case of smooth walls.

In an actual particle-laden turbulent flow, the fundamental understanding of the physics is complicated by the complex interplay between different phenomena: the dispersion of the particles by the flow, the forcing of the flow by the particles, inter-particle collisions, and particle–wall collisions. Therefore, in this study we consider a simplified well-defined situation: a non-uniform distribution of particles, kept at fixed positions in the 'bottom' part of the pipe, mimicking, in a way, the droplet distribution in the gas core of horizontal annular flow. The main objective of this study is to provide experimental evidence that the forcing of the flow by a non-uniform non-axisymmetric particle distribution, and the consequent turbulence modification, can promote secondary flow of the second kind in a fully developed turbulent pipe flow, and to understand the essential mechanisms associated with it. By keeping the particles fixed, the dispersion of the particles by the flow, inter-particle collisions and particle–wall collisions are eliminated, and the only phenomenon that remains is the forcing of the flow by the particles. Furthermore, with fixed particles, the only existing force in the cross-section is related to non-linear drag. However, as we will show below through an order of magnitude analysis, this force in the cross-section is much smaller than the drag in the streamwise direction, and since the changes in the Reynolds stresses in the cross-section are, to first-order, proportional to the streamwise forcing, the secondary flow is mainly driven by the non-uniform turbulence modification; as such, it is a secondary flow of the second kind.

Note that, although we are using a highly idealized configuration, it can represent to a certain extent some aspects present in real particle-laden flows, since the inelastic particle–wall collisions or the particle collisions with a rough wall lead, in real particle-laden flows, to a mean forcing of the flow in the axial direction. Note also that the droplets in horizontal annular flow break from the waves on the liquid film in the bottom, and are accelerated from roughly the wave velocity to the gas velocity; therefore, they induce a mean axial forcing of the flow in the bottom part of the gas core.

The rest of the paper is organized as follows. First, we briefly recall the theory regarding the driving mechanisms for secondary flow in fully developed turbulent flows in straight pipes. Then, we formulate the idealized problem and present the experimental set-up used to measure the particle-driven secondary flow. After, we present the results, focusing on (i) the relation between the occurrence of secondary flow and the turbulence modification caused by the non-uniform mean particle-forcing; and on (ii) a scaling law for particle-driven secondary flow.

2. Theory

In this section, we briefly recall the theory for the occurrence of secondary flow in single-phase flow (explained by Speziale 1982), and provide an extension for the case of particle-laden pipe flows. In particular, we clarify, in the presence of particle-forcing, which terms of the equations are associated with secondary flow of the first kind and which terms are associated with secondary flow of the second kind.

We consider a general situation consisting of a fully developed turbulent flow in a straight pipe of arbitrary cross-section, in a statistically steady situation (figure 2). By definition, the secondary flow is formed by the projection of the mean velocity field onto the pipe cross-section. Therefore, it is convenient to decompose the mean velocity field, $\boldsymbol{U}$, into a component parallel to the pipe cross-section, $\boldsymbol{V}$, and a streamwise component, $\boldsymbol{W}$:

$$\boldsymbol{U} \equiv \boldsymbol{V} + \boldsymbol{W}; \quad \boldsymbol{V} \equiv V_x \boldsymbol{e}_x + V_y \boldsymbol{e}_y; \quad \boldsymbol{W} \equiv W \boldsymbol{e}_z. \tag{2.1}$$

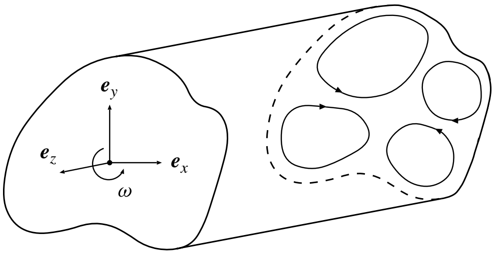

FIGURE 2. Fully-developed turbulent flow in a straight pipe of arbitrary cross-section.

The field $\boldsymbol{V}$ is by definition the secondary flow. Since we are considering a fully developed flow, $\boldsymbol{V}$ is determined by the averaged continuity and Navier–Stokes equations in the cross-section of the pipe, i.e. $\boldsymbol{V}$ is determined by the following two-dimensional equations:

$$\nabla \cdot \boldsymbol{V} = 0, \tag{2.2}$$

and

$$\rho \frac{\mathrm{D}\boldsymbol{V}}{\mathrm{D}t} = -\nabla \bar{P} + \mu \nabla^2 \boldsymbol{V} + \nabla \cdot \tilde{\boldsymbol{\tau}}, \tag{2.3}$$

where ρ is the density, μ is the viscosity, $\nabla \bar{P}$ is the projection of the gradient of the mean pressure onto the pipe cross-section, and $\tilde{\boldsymbol{\tau}}$ is the projection of the Reynolds stress tensor onto the pipe cross-section. Note that these are two-dimensional equations, and all vector and tensor operations/definitions are for a two-dimensional field. From (2.3), it is clear that the driving mechanism for the secondary flow is the divergence of $\tilde{\boldsymbol{\tau}}$.

By applying the curl to (2.3), we obtain the transport equation for the vorticity of $\boldsymbol{V}$, ω (since $\boldsymbol{V}$ is a two-dimensional field, ω is a scalar):

$$\rho \frac{\mathrm{D}\omega}{\mathrm{D}t} = \mu \nabla^2 \omega + \nabla \times (\nabla \cdot \tilde{\boldsymbol{\tau}}). \tag{2.4}$$

The secondary flow velocity, $\boldsymbol{V}$, can be obtained from the axial vorticity, ω, using the generalized Helmholtz decomposition for an incompressible flow in two dimensions (with the no-slip condition for $\boldsymbol{V}$ at the wall):

$$\boldsymbol{V}(\boldsymbol{x}_1) = \frac{1}{2\pi} \int_A \frac{\boldsymbol{r}(\boldsymbol{x}_1, \boldsymbol{x}_2)}{r^2(\boldsymbol{x}_1, \boldsymbol{x}_2)} \times \omega(\boldsymbol{x}_2)\, \boldsymbol{e}_z \, \mathrm{d}A(\boldsymbol{x}_2), \tag{2.5}$$

where A is the area of the cross-section, $\boldsymbol{x}_1$ and $\boldsymbol{x}_2$ are position vectors in the cross-section, and $\boldsymbol{r}(\boldsymbol{x}_1, \boldsymbol{x}_2)$ is the distance vector between $\boldsymbol{x}_1$ and $\boldsymbol{x}_2$ (i.e. $\boldsymbol{r}(\boldsymbol{x}_1, \boldsymbol{x}_2) = \boldsymbol{x}_2 - \boldsymbol{x}_1$). From (2.4), it is clear that $\nabla \times (\nabla \cdot \tilde{\boldsymbol{\tau}})$ is the source term for ω; therefore, it follows that a necessary and sufficient condition for the existence of a secondary flow of the second kind in single-phase pipe flow is

$$\nabla \times (\nabla \cdot \tilde{\boldsymbol{\tau}}) \neq 0. \tag{2.6}$$

Above, we did not consider any forcing of the flow, for example, by particles. If a forcing is added, then (2.3) and (2.4) become

$$\rho \frac{\mathrm{D}\boldsymbol{V}}{\mathrm{D}t} = -\nabla \bar{P} + \mu \nabla^2 \boldsymbol{V} + \nabla \cdot \tilde{\boldsymbol{\tau}} + \boldsymbol{\Phi}, \tag{2.7}$$

and

$$\rho \frac{D\omega}{Dt} = \mu \nabla^2 \omega + \nabla \times (\nabla \cdot \tilde{\boldsymbol{\tau}}) + \nabla \times \boldsymbol{\Phi}, \tag{2.8}$$

where $\boldsymbol{\Phi}$ is the projection of the average forcing per unit of volume, $\langle \mathfrak{F} \rangle$, onto the pipe cross-section:

$$\boldsymbol{\Phi} \equiv \langle \mathfrak{F} \rangle - \bar{\mathfrak{F}}_z \boldsymbol{e}_z; \quad \bar{\mathfrak{F}}_z \equiv \langle \mathfrak{F} \rangle \cdot \boldsymbol{e}_z. \tag{2.9}$$

In order to analyse the relation between the forcing and the existence of secondary flow, it is convenient to decompose $\boldsymbol{\Phi}$ into two parts: one independent of the secondary flow, $\boldsymbol{\Phi}_o$, and one dependent of the secondary flow, $\boldsymbol{\Phi}_v$, i.e. we define

$$\boldsymbol{\Phi}_v \equiv \boldsymbol{\Phi} - \boldsymbol{\Phi}_o; \quad \boldsymbol{\Phi}_o \equiv \boldsymbol{\Phi}(\boldsymbol{V} = 0). \tag{2.10}$$

From (2.7) and (2.8), it becomes clear that $\boldsymbol{\Phi}_o$ and $\nabla \cdot \tilde{\boldsymbol{\tau}}$ are the driving mechanisms for the secondary flow, and the necessary and sufficient condition for the existence of secondary flow in particle-laden pipe flows is

$$\nabla \times (\nabla \cdot \tilde{\boldsymbol{\tau}}) + \nabla \times \boldsymbol{\Phi}_o \neq 0. \tag{2.11}$$

In turbulent flows, it is possible to have a large forcing with zero $\boldsymbol{\Phi}_o$. For example, if the forcing is proportional to the fluid velocity, which would be the case for a fixed distribution of particles with linear drag. If $\boldsymbol{\Phi}_o$ is equal to zero, then condition (2.6) remains the necessary and sufficient condition for the existence of secondary flow. In the case of moving particles and/or non-linear drag, $\boldsymbol{\Phi}_o$ is not necessarily equal to zero, and it can, in principle, induce a secondary flow.

In single-phase flow, it is usual to make a distinction between secondary flow of the first kind and secondary flow of the second kind. A similar distinction can be made for particle-laden flows. A secondary flow driven by $\nabla \times \boldsymbol{\Phi}_o$ in (2.11) corresponds to a secondary flow of the first kind. A secondary flow driven by $\nabla \times (\nabla \cdot \tilde{\boldsymbol{\tau}})$ in (2.11), promoted in this case 'indirectly' by the non-uniform particle-forcing, corresponds to a secondary flow of the second kind.

3. Problem formulation

We would like to show that non-uniformly distributed particles in a turbulent pipe flow can generate a secondary flow of the second kind, through the non-uniform turbulence modification the particles induce. To do so, we consider a very simple and well-defined test case: a non-uniform distribution of particles kept at fixed positions. The distribution of the fixed particles in the measurements is shown in figure 3. This idealized configuration allows us to isolate the effects of the axial forcing on the turbulence, in order to better understand how this forcing can promote a secondary flow of the second kind. With fixed particles, the only mean forcing in the cross-section is due to non-linear drag.

Indeed, the particle Reynolds number, Re_p, is quite high because the particles have a finite size and are kept at fixed positions in our experiments. Therefore, the particle-forcing on the flow is non-linear. Due to the turbulence velocity fluctuations, the non-linear drag force results in a component in the cross-section, even in the absence

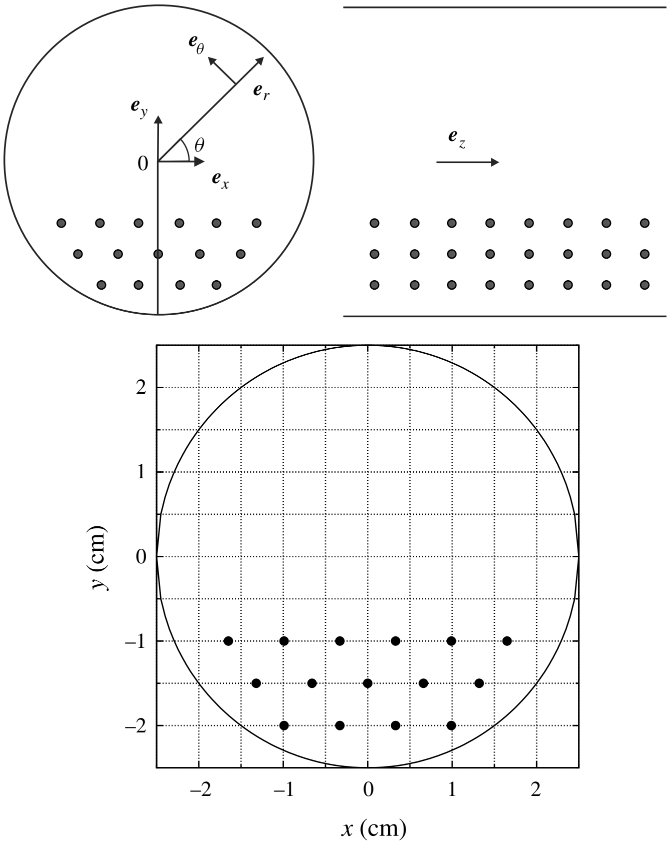

FIGURE 3. Coordinate system and distribution of the fixed particles.

of secondary flow. This component, $\boldsymbol{\Phi}_o$, is proportional to the Reynolds shear-stresses $\overline{u_x u_z}$ and $\overline{u_y u_z}$, in the x and y directions, respectively. However, the forcing in the cross-section due to non-linear drag is small compared with the axial forcing:

$$\frac{\Phi_o}{|\bar{\mathfrak{F}}_z|} \sim \left(\frac{u_\nabla}{u_B}\right)^2, \tag{3.1}$$

where u_B is the bulk velocity, and u_∇ is the friction velocity based on the mean pressure-gradient in the axial direction, $-\nabla \bar{P}_z$:

$$u_\nabla \equiv \left(\frac{-\nabla \bar{P}_z}{\rho}\frac{D}{4}\right)^{0.5}. \tag{3.2}$$

We show in the results that the divergence of the Reynolds-stress tensor in the cross-section, $\nabla \cdot \tilde{\boldsymbol{\tau}}$, scales with the particle-forcing in the axial direction; therefore,

$$\frac{\Phi_o}{|\nabla \cdot \tilde{\boldsymbol{\tau}}|} \sim \left(\frac{u_\nabla}{u_B}\right)^2. \tag{3.3}$$

Since the bulk velocity is much larger than the friction velocity, the particle-forcing in the cross-section due to non-linear drag, $\boldsymbol{\Phi}_o$, has a negligible effect when compared

	'Low'	'High'
Re_B in LDA experiments with fixed particles	5494	10 864
Re_B in LDA experiments without particles	5600	9745
Re_B in DNS/LES simulations without particles	5300	10 600
D	0.05 m	0.05 m
D_p	1 mm	1 mm
$\mathscr{L}_t$	4.4 mm	4.1 mm
$\mathscr{L}_k$	218 μm	135 μm
D_p/D	0.02	0.02
$\mathscr{L}_t/D$	0.09	0.08
$D_p/\mathscr{L}_t$	0.23	0.24
$D_p/\mathscr{L}_k$	4.6	7.4

TABLE 1. Flow conditions at the 'low' and 'high' bulk Reynolds numbers. Note that the turbulence length scales are estimated at the bulk Reynolds number of the simulations.

with the effect of the turbulence modification promoted by the axial forcing; hence, secondary flow of the first kind is negligible.

The influence of the particle-forcing on the flow is studied by considering two bulk Reynolds numbers, $Re_B \approx 5300$ and $Re_B \approx 10\,600$, which we denote by 'low' and 'high' bulk Reynolds numbers, respectively. Single-phase pipe flow experiments (without particles) are also performed at approximately the same bulk Reynolds numbers, in order to provide comparison data for the flow with and without particles. Furthermore, the single-phase pipe flow experiments (without particles) are compared with results of direct numerical simulation (DNS) and large-eddy simulation (LES), at approximately the same bulk Reynolds numbers (DNS for the 'low' bulk Reynolds number and LES for the 'large' bulk Reynolds number). The bulk Reynolds numbers are shown in table 1. The values for the laser Doppler anemometry (LDA) experiments are based on the mean mass flow-rate and the kinematic viscosity at the mean temperature of the experiments. The DNS and LES are performed at a friction Reynolds number, Re_∇, of 360 and 660, for the 'low' and 'high' bulk Reynolds numbers, respectively. Details on the DNS and LES can be found in Eggels *et al.* (1994) and Portela, Cota & Oliemans (2002).

The fixed particles are distributed more or less uniformly in the bottom part of the pipe, as sketched in figure 3. The distance between two neighbour particles in the axial direction is $L_p^z = 0.1D$, with D being the pipe diameter. In the cross-section, the particles are distributed in three layers, at $0.1D$, $0.2D$ and $0.3D$ from the pipe bottom. The three layers have, respectively, four, five and six particles in the cross-section plane. The distance between two neighbour particles in the cross-section plane is equal to $L_p^c = 0.132D$.

The different length scales are summarized in table 1. In the table, D_p is the particle diameter, $\mathscr{L}_t = k^{3/2}/\epsilon$ is the length scale representative of the large turbulence scales and $\mathscr{L}_k$ is the Kolmogorov length scale. In the calculation of the turbulence length scales, ϵ is the average turbulence dissipation and it is computed using the Blasius friction relation. It is important to note that the particle diameter is smaller than $\mathscr{L}_t$, but that it is larger than the Kolmogorov length scale, $\mathscr{L}_k$. Therefore, 'direct' effects of the particles on the turbulence modification can be expected in the experiments.

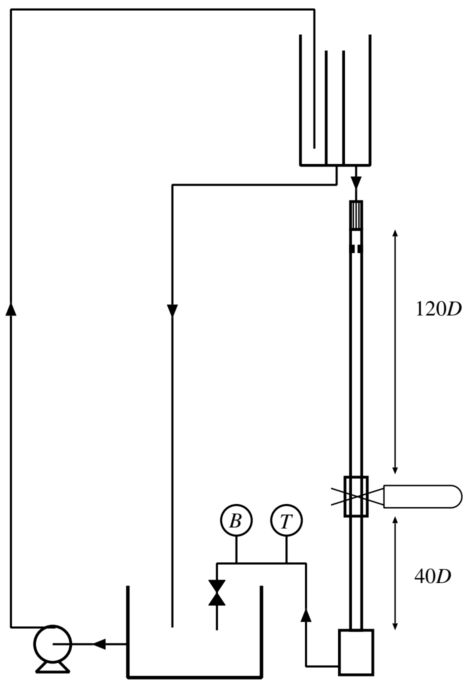

FIGURE 4. Experimental set-up. At T, the temperature is measured. At B, the mass flow rate can be measured with a balance.

4. LDA experiments

4.1. *Experimental set-up*

The present experiments are done in a closed circuit water loop (figure 4). The main part of the loop consists of a vertical cylindrical pipe made of Perspex, with an inner diameter of $D = 0.05$ m and a length of roughly 9 m. Smooth entrance conditions are made by feeding the pipe of water through an overflow vessel. At the entrance of the pipe, water passes through a flow straightener in order to suppress large swirl motions, after which it is tripped by a trip ring. The measurement section is approximately 6 m downstream of the entrance, leaving roughly 120D for the turbulent flow to develop. After the measurement section, approximately 2 m (40D) are left in order to avoid exit effects in the measurement section. At the exit of the pipe, the water flows back into a large reservoir, from which it is pumped back to the overflow vessel. The mass flow rate is measured at the exit of the pipe using a bucket and a balance. The water temperature is measured at the exit of the pipe. During each measurement set (i.e. one Reynolds number, with or without fixed particles), the temperature variation was less than 2.5 °C; therefore, the variations in the water density, ρ, and viscosity, μ, were negligible in each measurement set. The values of ρ and μ were obtained from handbook tables, at the mean temperature in the measurement set, which allowed us to get an accurate estimation of the actual Reynolds number.

The curvature of the pipe wall, together with the difference in refractive index between water, Perspex, and air, leads to difficulties in the positioning and alignment of the LDA measurement volume along the x- and y-axes in the vicinity of the wall (see figure 3 for the definition of the coordinate system). To solve this, the measurement section is made of a circular Perspex pipe with a thin wall of 1 mm

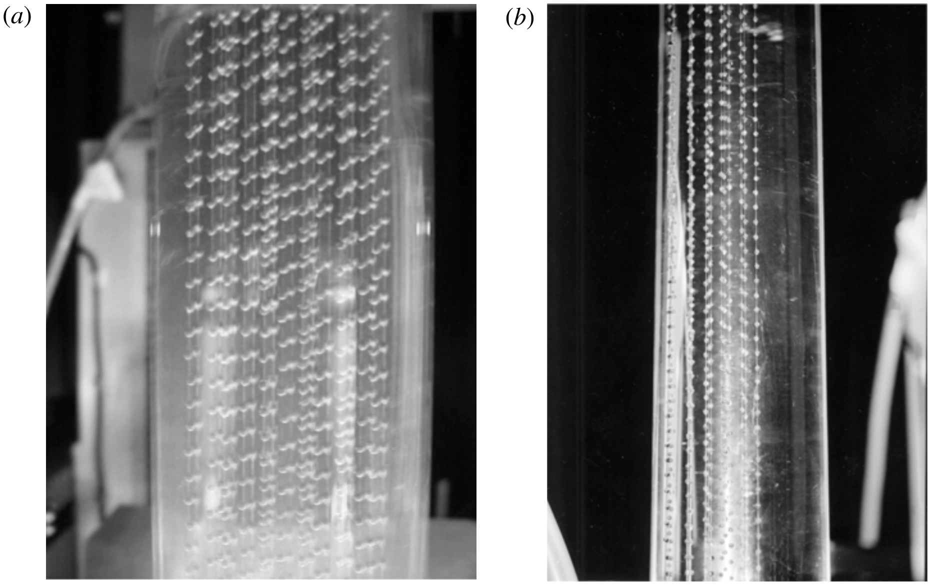

FIGURE 5. Photos of the particles on lines in the pipe. A view from the 'bottom' (along the y-axis) (*a*). A view at an angle between the 'bottom' and the 'side' (*b*).

thickness and with an inner diameter of exactly $D = 0.05$ m. Furthermore, a squared box filled with water is placed over the measurement section.

In the particle-driven secondary flow experiments, the actual distribution of the fixed particles is shown in figure 5. To keep the particles at their fixed positions, the lead particles of 1 mm diameter are put every 5 mm on a 0.1 mm line. The lines are attached on bars traversing the pipe below the trip ring, and are put under stress at the pipe exit through a tightening mechanism, in order to maintain them at the desired position. The maximum stress that could be put on the lines was sufficient to avoid vibrations of the lines at the relatively low Reynolds numbers used in this study; however, it did not allow us to go to higher Reynolds numbers, otherwise vibrations would be observed.

Below, in the explanation of the results, we refer, for simplicity, to the region where $y < 0$ as the bottom part of the pipe, and to the region where $y > 0$ as the top part of the pipe.

4.2. *LDA set-up*

Velocity measurements are made using a standard two-component backscatter LDA TSI-system (4 W Spectra-Physics AR^+ laser, TSI 9201 colourburst beam separator and TSI 9203 colourlink downmixer). The output signal from the LDA system is processed using a TSI IFA-750 processor. The length and width of the measurement volume are roughly equal to 250 and 40 µm, respectively. When comparing these values with the Kolmogorov length scales in table 1, it can be seen that the velocity of the smallest scales in the flow can be measured. The velocity signal is measured for 300 s at the measurement location, giving on average a set of samples larger than 3×10^4 values in both directions. For the tracer particles, we used TSI spherical glass hollow beads, with a diameter of 8–12 μm and a density close to the water density (≈1.05–1.15 × 10^3 kg m^{-3}).

The velocity components measured with LDA are in the plane of the laser beams pair, and normal to the bisector of the two laser beams. Since the secondary flow velocity is at least one order of magnitude smaller than the axial velocity, the alignment of the laser beams plane along the x-, y- and z-axes is crucial, in order to avoid a 'leakage' from the axial velocity component to the cross-sectional velocity components. The alignment procedure consists of three steps, which allowed us to measure the secondary flow with a good accuracy, as shown in the results. The LDA probe is aligned by (i) aligning the plane of the laser beam pairs with the plane of their reflections, (ii) aligning the plane of the laser beams pair for the axial velocity component with the pipe wall, and (iii) checking that symmetric velocity components in the cross-section are very small on the symmetry axis.

The LDA probe is mounted on a traversing system in all directions, within an accuracy of ±5 μm. However, the absolute positioning of the measurement volume in the pipe is not known with LDA, since the exact position of the wall is unknown. A first guess of the wall position is obtained by traversing and searching at zero fluid flow for a signal with a high noise level due to reflections of a scattering particle on/in the wall. Then, the wall position, on the x- and y-axes in the single-phase flow experiments and on the x-axis in the particle-driven secondary flow experiments, is corrected for by computing the symmetry axis in the profiles of the mean or root-mean-square (r.m.s.) velocity, knowing the exact value of the pipe diameter.

LDA data are subject to a variety of bias errors (Absil 1995; Tummers 1999; Van Maanen 1999). The results presented in this study are corrected for the largest sources of bias errors: (i) velocity bias, (ii) multiple validation, and (iii) noise. Velocity bias results from the larger probability to sample the velocity of a tracer particle moving with a large velocity through the measurement volume. Therefore, statistical quantities computed as arithmetic averages will be erroneous. The inter-arrival time weighting is used to compensate for the velocity bias, which is valid, since the criterion $\dot{N} \approx 10/\lambda_T$, where $\dot{N}$ is the mean data rate and λ_T the Taylor time scale, is met (Tummers 1999). The velocity bias correction of the data is found to be small (≈1.5 % on average, with a maximum correction close to the wall in the order of ≈5 %). Multiple validation occurs when the burst generated by one tracer particle is detected as generated by more than one tracer particle (Van Maanen 1999). This is corrected for by introducing a 'dead time' after the detection of a tracer particle in the post-processing. It is verified that multiple validation has been removed by considering the Poisson distribution of the inter-arrival time probability distribution. Also, the multiple validation correction is found to be negligible ($\ll$1 %, except very close to the wall, $\ell \lessapprox 0.8$ mm, where it can be in the order of ≈3 %).

Noise in the experiments can contribute to the value of the velocity variance, since the variance of noise, $\overline{n^2}$, is not equal to zero:

$$\overline{(u+n)^2} = \overline{u^2} + \overline{n^2}. \tag{4.1}$$

In our LDA system, operating in backscatter mode, noise can account for approximately 10–20 % of the variance; therefore, it must be removed in the post-processing. It is assumed that noise is uncorrelated in time. Therefore, noise has only a contribution to the time autocorrelation function at zero time lag, and the autocorrelation function does not tend to unity in the limit of zero time lag. An extrapolation of the fit of the autocorrelation function at zero time lag gives an estimate for the noise-free part of the velocity variance. Due to the irregular distribution in time of the velocity samples, the autocorrelation coefficient is estimated using a local normalization fuzzy slotting technique with local time estimation (Tummers 1999; Van Maanen 1999; Benedict, Nobach & Tropea 2000; Nobach 2002; Harteveld 2005). We use the model-based fit of the autocorrelation coefficient proposed by Nobach (2002):

$$R_k = ac\exp(-bk) - ab\exp(-ck), \tag{4.2}$$

where R_k is the autocorrelation coefficient with lag k, and a, b, and c are the model parameters to fit. The model-based fit is verified to be adequate, and has the advantage of giving an estimate of the Taylor time scale: $\lambda_T = (2/(bc))^{0.5}$. The expression for the variance of the autocorrelation coefficients, as proposed by Tummers (1999), is used as weighting function in the fit. Details on the procedure in the estimation of the noise-free variance can be found in Daalmans (2005).

The Reynolds shear stresses are measured by applying a simultaneity criterion (through a coincidence window) on the time signal during post-processing. The coincidence window is set to 200 and 350 μs, for the 'high' and 'low' Reynolds numbers, respectively, which is smaller than the mean inter-arrival time and larger than the mean transit time. Finally, the samples in the data set with a velocity larger/smaller than the mean velocity ± 5 times the standard deviation are considered as outliers and are rejected. This correction did not influence much the statistical quantities ($<1\,\%$). Other possible sources of bias errors are insignificant in our measurement set-up and are not corrected for.

5. Results of single-phase turbulent pipe flow (without particles)

To ensure that we can measure with a reasonable accuracy the secondary flow velocity and the Reynolds stresses in the cross-section, we compare in this section reference measurements of single-phase turbulent pipe flow (without particles) with DNS/LES at roughly the same Reynolds numbers. The actual bulk Reynolds numbers are given in table 1. Although the values of the bulk Reynolds numbers are slightly different in the LDA experiments and DNS/LES, we do not expect significant differences in the turbulence properties when they are normalized with the friction velocity, u_∇.

As explained above, the centre of the pipe and the wall position are determined by determining the symmetry axis in the profiles. Since the measured profiles are very symmetric, we present in the results the average of the two halves of the profiles. The results shown for the single-phase turbulent pipe flow are normalized by the friction velocity, u_∇. In the experiments, u_∇ is determined from the mass flow rate obtained from the LDA results and the Blasius relation.

The mean axial velocity profile is shown in figure 6. The experimental and numerical results coincide very well all over the pipe, except very close to the wall (for $\ell \lessapprox 0.8$ mm from the wall). The flow rate obtained by integration of the mean axial velocity profile gives an error of roughly $-2.5\,\%$, when compared with the flow rate measured with a balance.

The profiles of the experimentally measured radial and tangential mean velocities, normalized with the local axial velocity, are shown in figure 7. The radial and tangential velocities are very small compared with the local axial velocity, except very close to the wall. Over a large part of the pipe cross-section, the ratio of the cross-sectional velocity to the axial velocity is smaller than 0.2 %, which is one

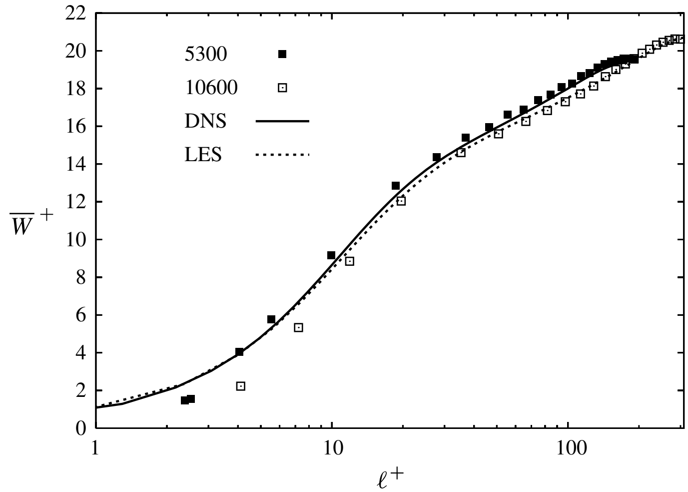

FIGURE 6. Mean axial velocity as a function of the distance to the wall (in wall units), for the single-phase pipe flow experiments at the 'low' and 'high' bulk Reynolds numbers. The symbols correspond to the experimental results (closed and open symbols for the 'low' and 'high' bulk Reynolds numbers, respectively), and the lines correspond to the simulation results (solid and dashed lines for the 'low' and 'high' bulk Reynolds numbers, respectively).

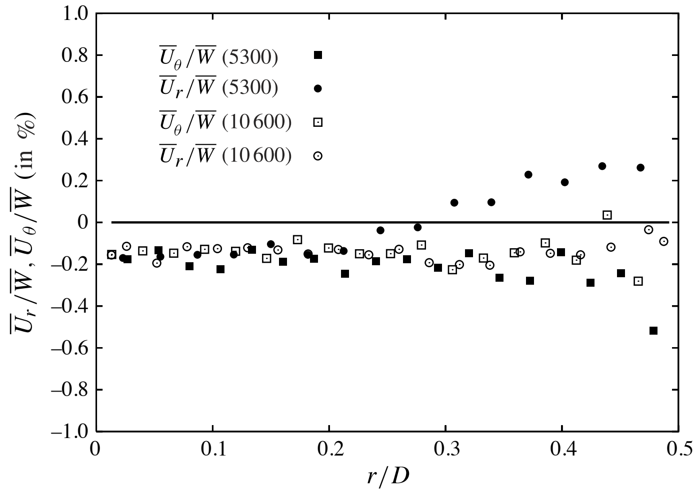

FIGURE 7. Cross-sectional velocities (in percentage of the mean local axial-velocity), as a function of the pipe radius, for the single-phase pipe flow experiments. The closed and open symbols correspond to the 'low' and 'high' bulk Reynolds numbers, respectively. The squares and circles correspond to the mean tangential and radial velocities, respectively.

order of magnitude smaller than the expected secondary flow velocity promoted by the particle-forcing. However, very close to the wall (i.e. for the first or second measurement points from the wall), the mean axial velocity is also small, and the error can be larger. In figure 7, these points are outside of the figure, and are not shown for readability reasons. Consequently, the particle-driven secondary flow can be

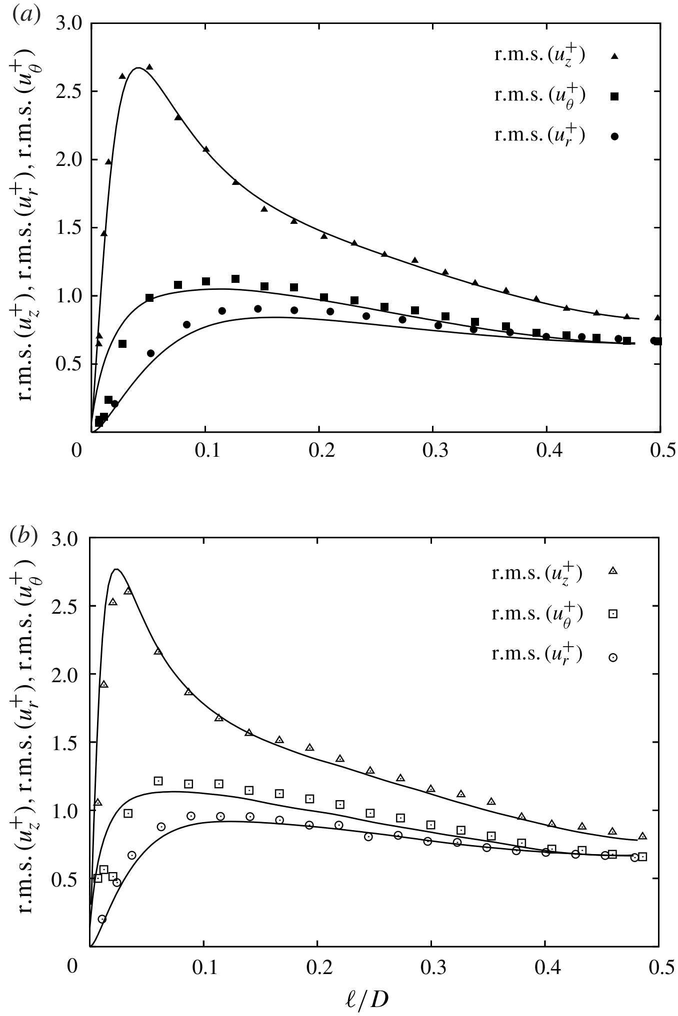

FIGURE 8. Velocity fluctuations (in wall units), as a function of the distance to the wall, for the single-phase pipe flow at the 'low' (*a*) and 'high' (*b*) bulk Reynolds numbers. The symbols correspond to the experiments (the squares, circles and triangles correspond to the tangential, radial and axial velocity fluctuations, respectively) and the lines to the simulations (DNS for the 'low' and LES for the 'high' bulk Reynolds number).

measured within a good accuracy in the major part of the cross-section. Furthermore, the ratio of the cross-sectional velocity to the axial velocity is constant (except for the radial one at the 'low' bulk Reynolds number), indicating that it is caused by a small misalignment of the measurement volume, in the order of 0.1°.

The profiles of the turbulence velocity fluctuations are shown in figure 8. The velocity fluctuations in the experiments and simulations are in good agreement, especially in the central region; the difference being less than 5 %. The cross-sectional velocity fluctuations are more difficult to measure accurately close to the wall, where, however, the trend and the order of magnitude is still correctly measured. Hence, with the present results, we show that we can measure accurately the changes in the cross-

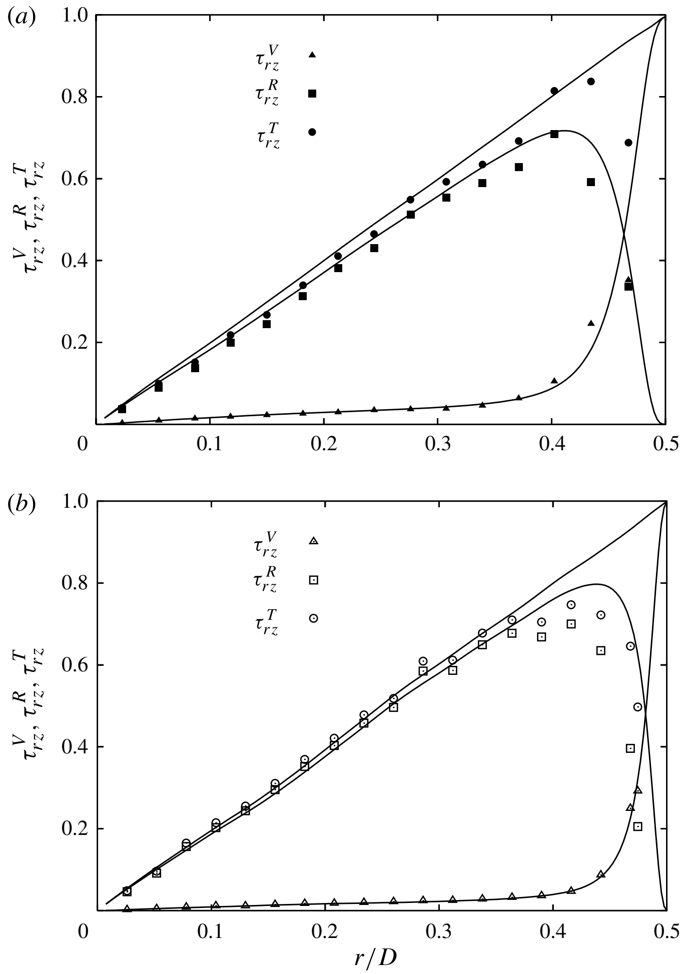

FIGURE 9. Reynolds, viscous and total shear-stresses (in wall units), as a function of the radial position, for the single-phase pipe flow at the 'low' (a) and 'high' (b) bulk Reynolds numbers. The symbols correspond to the experiments (the circles, squares and triangles correspond to the total shear stress, τ^T_{rz}, Reynolds shear stress, τ^R_{rz}, and viscous shear stress, τ^V_{rz}, respectively) and the lines to the simulations (DNS for the 'low' and LES for the 'high' bulk Reynolds number).

sectional velocity fluctuations due to particle-forcing, when the changes, compared with single-phase pipe flow, are larger than roughly 7 % ($\approx\sqrt{25}$ %) of the velocity fluctuations.

The profiles of the viscous, Reynolds and total shear stresses are shown in figure 9. Again, the agreement between experiments and simulations is good in the centre of the pipe. The total stress is linear over all of the pipe, except close to the wall (for $r/D \gtrapprox 0.4$), where the discrepancy can be explained by non-overlapping measurement volumes due to refraction at the curved wall. It can be observed that the slope of the total shear stress is close to 2. This means that the normalization of the shear stresses by the friction velocity squared, u_∇^2, computed from the Blasius relation with the bulk velocity, u_B, obtained from the LDA measurements, is correctly predicted.

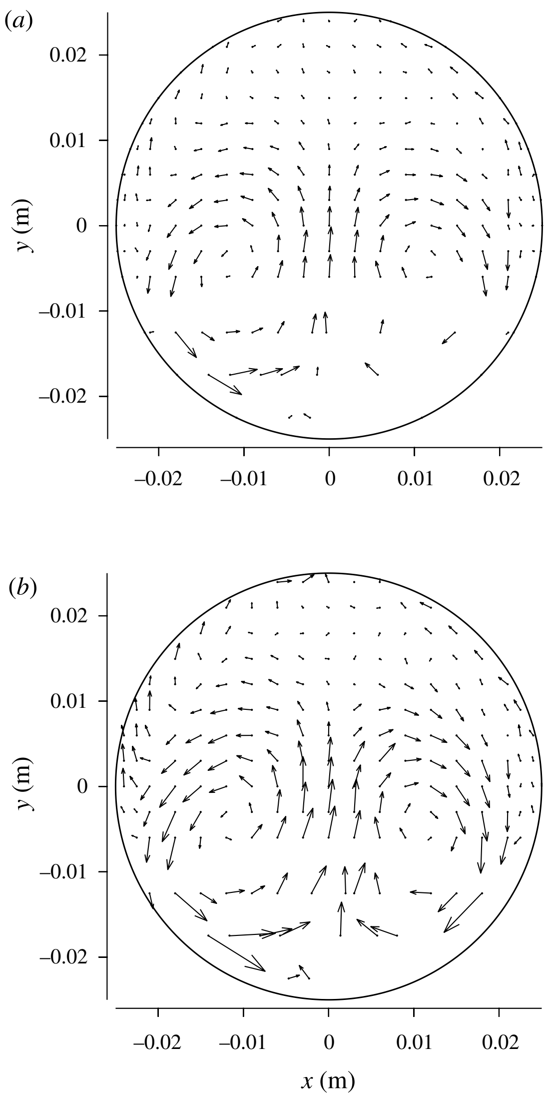

FIGURE 10. Vector field of the secondary flow velocity for the 'low' (*a*) and 'high' (*b*) bulk Reynolds numbers. The normalization of the vectors is the same in both figures. Note that the missing vectors in the bottom part of the pipe are due to the blockage of the laser beams by the fixed particles.

6. Particle-driven secondary flow

6.1. *Secondary flow velocity*

The particle-driven secondary flow measurements are shown in this section. They are performed at roughly the same bulk Reynolds number as in the reference measurements of single-phase turbulent pipe flow (without particles) presented in the preceding section. The actual bulk Reynolds numbers are given in table 1.

The velocity vector field in the cross-section is shown in figure 10. We do observe the occurrence of particle-driven secondary flow in figure 10, for the two bulk Reynolds numbers. The secondary flow consists of (i) two large cells in the pipe bottom, which are perfectly symmetric with respect to the y-axis and of large amplitude; and (ii) two elongated cells in the top of the cross-section, which are symmetric with respect to the y-axis and of small amplitude. The two large cells in the bottom flow downward along the wall and upward on the y-axis, whereas the elongated cells in the top flow in the opposite direction, i.e. upward along the wall. The presence of at least two secondary flow cells is explained by symmetry, since the mean circumferential velocity must be zero on the y-axis, which is the symmetry axis of the experimental set-up. Furthermore, we observe that the secondary flow pattern is exactly the same at the 'low' and 'high' bulk Reynolds numbers, but the velocity differs in amplitude. We can note that the direction of the two large cells in the bottom is the same as that reported by Dykhno *et al.* (1994) in horizontal gas–liquid annular flow when droplets are ejected from the liquid film.

The norm of the secondary flow velocity is shown in figure 11. We can see that the magnitude of the secondary flow velocity is significant, with a maximum amplitude up to 9 % of the bulk velocity, u_B. Furthermore, we can see that the differences in the norm of the secondary flow velocity between the 'low' and 'high' bulk Reynolds numbers are small, when normalized with the bulk velocity, u_B. This suggests that the particle-driven secondary flow scales roughly with Re_B^{α}, with α in the order of one. Such a scaling has also been suggested for secondary flow in non-circular pipes, where it seems to scale with Re_{∇} (Brundrett & Baines 1964; Launder & Ying 1972), which, in turn, scales globally with Re_B^{α}. The least-squares proportionality constant between the secondary flow velocities at the 'low' and 'high' bulk Reynolds numbers is equal to roughly 1.51, which corresponds to a value of α equal to 0.59. In § 7, we show that the measured proportionality constant of 1.51 is close to that obtained from a scaling law based on dimensional analysis.

The white contours in figure 11 correspond to values of the norm of the secondary flow velocity lower than 0.5 % of the bulk velocity, which is an estimation of the measurement error in the cross-sectional velocities in the case of the measurements with particles (see the discussion below). The fact that a large part of the vectors in figure 10 are larger than the measurement error confirms that we have four secondary flow cells in the cross-section.

In fully developed flow, the net transport of mass by secondary flow through the x- and y-axes must be equal to zero. We show in figures 12 and 13 the profiles of the secondary flow velocity components in the y and x directions along the x- and y-axes, respectively. Therefore, ideally, the net integral of the curves in figures 12 and 13 must be equal to zero. We can see that, indeed, the net integral is small. Normalized with the transport of mass by the mean axial flow on the same x- or y-axis, the net transport of mass by secondary flow is less than 0.5 %, which gives an estimation of the measurement error. This measurement error is slightly larger than in single-phase flow (without particles). In single-phase flow, we verified the alignment *a priori* (by also checking that the measured velocity in the cross-section was very small), which could not be done for the measurements with particle-driven secondary flow. Moreover, in figure 13, the secondary flow component V_x must be small, since the y-axis is an axis of symmetry, if the fixed particles are perfectly positioned. It can be seen that, indeed, V_x on the y-axis is much smaller than the maximum secondary flow velocity that was measured. Therefore, below, we will use the y-axis as a true axis of symmetry.

6.2. *Mean axial velocity and Reynolds shear stress*

The contours of the mean axial velocity are shown in figure 14. They show that the mean axial velocity has a good symmetry with respect to the y-axis, and that the

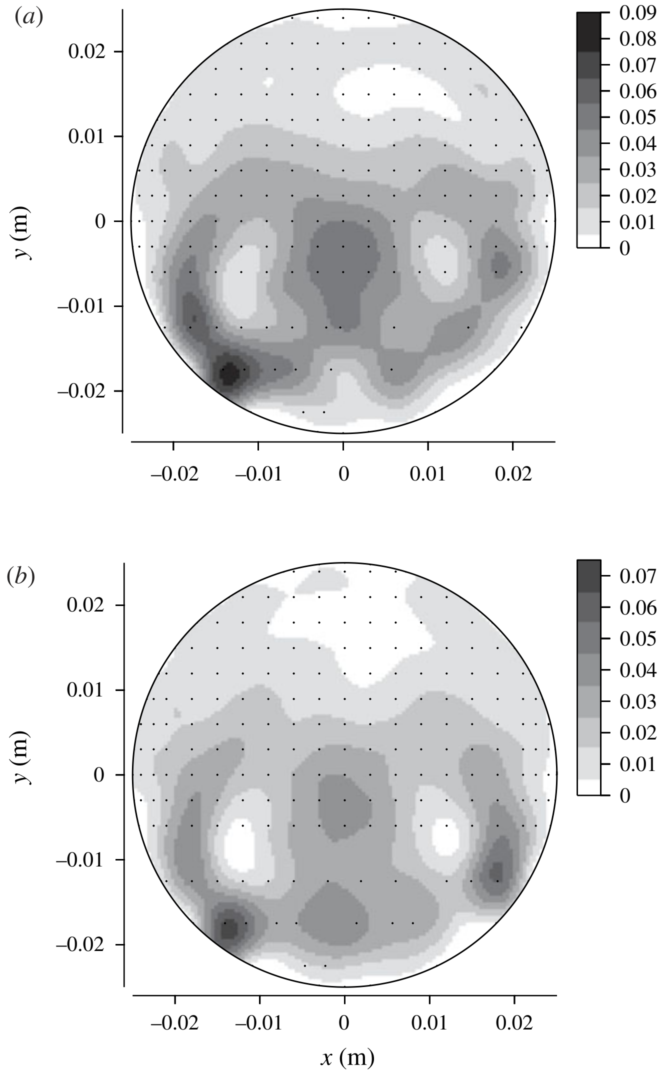

FIGURE 11. Norm of the secondary flow velocity for the 'low' (*a*) and 'high' (*b*) bulk Reynolds numbers, made dimensionless with the bulk velocity, u_B. Note that in the bottom-right part of the cross-section ($x \geqslant 0$ and $y \leqslant -0.01$ m) the grid in the measurements is quite large, due to the blockage of the laser beams by the fixed particles; therefore, the contours in the bottom-right part of the cross-section are rough.

particle-forcing produces a large shift of the maximum velocity toward the top of the cross-section. This shift in the mean axial velocity is in the same direction as that of the secondary flow velocity on the y-axis in the bottom part of the cross-section.

In the case of pipe flows with no internal forcing and uniform boundary conditions, such as in pipes of non-circular cross-section, the shift in the mean axial velocity gives the secondary flow direction. For instance, in a square pipe, it has been observed that the iso-velocity lines are displaced toward the corners, which can be explained with a simple balance of momentum in the axial direction. Due to secondary flow, there is a net flow of momentum toward the corner, which needs

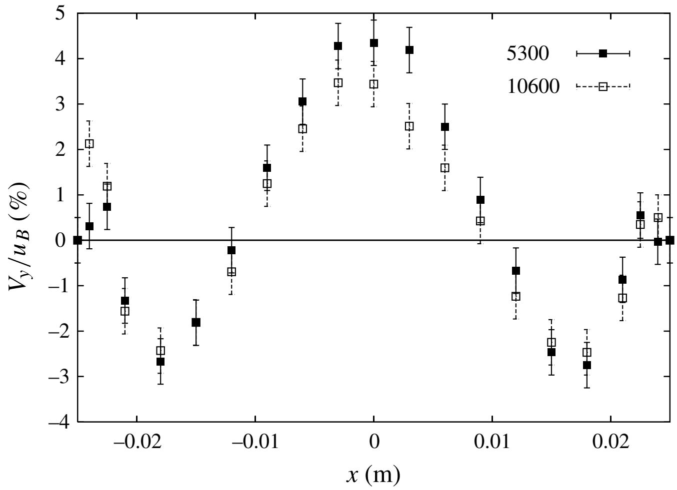

FIGURE 12. Profile of the mean vertical velocity, $\overline{V}_y$, on the x-axis, made dimensionless with the bulk velocity, u_B, for the 'low' (closed symbols) and 'high' (open symbols) bulk Reynolds numbers. The error bars represent the measurement error, which is estimated to be equal to roughly 0.5 %.

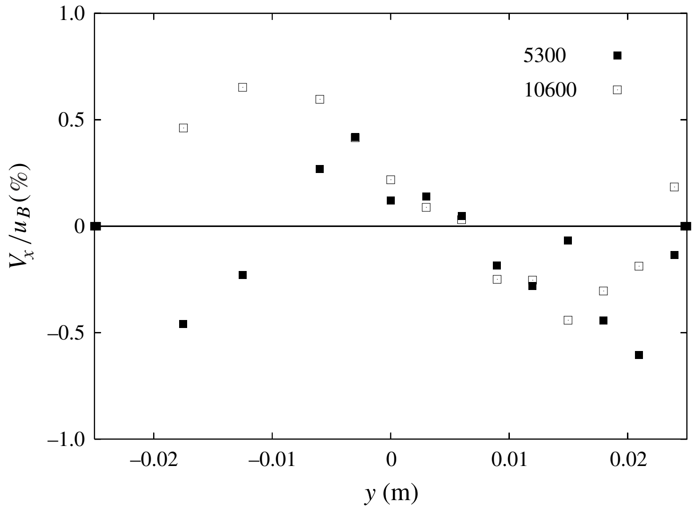

FIGURE 13. Profile of the mean horizontal velocity, $\overline{V}_x$, on the y-axis, made dimensionless with the bulk velocity, u_B, for the 'low' (closed symbols) and 'high' (open symbols) bulk Reynolds numbers.

to be balanced by an increase of the shear stress along the bisector line, which, in turn, leads to an increase in the mean axial velocity in the corner. However, in the case of internal forcing and/or non-uniform boundary conditions, the secondary flow direction cannot be inferred directly from the shift in the mean axial velocity. The internal forcing and/or non-uniform boundary conditions introduce changes in the momentum balance in the axial direction, which are not related to the occurrence

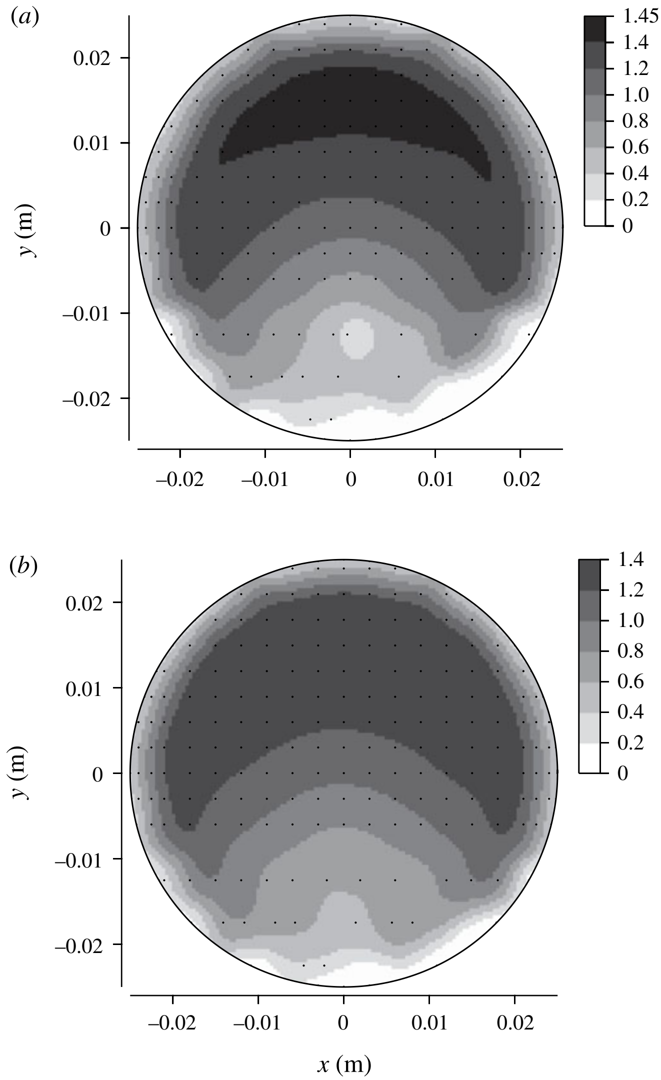

FIGURE 14. Contours of the mean axial velocity, normalized with the bulk velocity, u_B, for the 'low' (*a*) and 'high' (*b*) bulk Reynolds numbers.

of secondary flow, and which also lead to a modification of the mean axial velocity pattern.

In the absence of secondary flow, or for a negligible flow of axial momentum due to secondary flow, the balance of axial momentum on the y-axis gives

$$0 = -\nabla \bar{P}_z + \bar{\mathfrak{F}}_z + \frac{\partial \tau_{yz}^T}{\partial y}, \tag{6.1}$$

where $-\nabla \bar{P}_z$ is the mean pressure gradient in the axial direction, $\bar{\mathfrak{F}}_z$ is the mean axial forcing ($\bar{\mathfrak{F}}_z < 0$ in our case), and τ_{yz}^T is the total shear stress. We consider the case of an internal forcing far from the wall in the bottom part of the cross-section, as in our experiments. In fully developed flow, the mean pressure gradient in the axial direction is constant over the cross-section, therefore, the mean axial forcing must be compensated by a decrease in the total shear-stress gradient, which, far from the wall, is mostly equal to the Reynolds shear-stress gradient. Consequently, for the non-uniform forcing, the Reynolds shear-stress gradient is lower in the bottom part, when compared with the top part of the cross-section.

For a forcing far from the wall (in the outer layer), the turbulence dynamics close to the wall (in the inner layer) remains unaffected. This corresponds to Townsend's Reynolds number similarity hypothesis (Townsend 1976), except that the forcing in our case is in the outer layer, instead of in the inner layer as in the case of roughness. Therefore, the turbulence close to the wall behaves irrespective of the forcing far from the wall, with the only constraint being to match the Reynolds shear-stress gradient far from the wall. Consequently, for the non-uniform forcing, the total shear-stress gradient close to the bottom wall is lower than close to the top wall. Close to the wall, the viscous shear stress contributes most of the total shear stress. Hence, for the non-uniform forcing, the mean axial velocity is lower in the bottom of the pipe. This is verified by the contours in figure 14. Below, this mechanism is referred to as the 'blockage' effect.

Figure 14 shows a large distortion of the mean axial velocity field. In the next section, we see that this has a large impact on the production of turbulence kinetic energy (TKE). Close to the wall, the gradient of the mean axial velocity in the radial direction is decreased in the bottom part, when compared with the top part of the cross-section. Farther from the wall, the gradient of the mean axial velocity in the radial direction becomes larger in the bottom part than in the top part of the cross-section, due to the shift of the mean axial velocity profile toward the top. Figure 14 also shows the occurrence of gradients of the mean axial velocity in the circumferential direction, in the bottom part of the cross-section.

The contours of the Reynolds shear stress, $-\rho\,\overline{u_r u_z}$, are shown in figure 15. It is computed from

$$\overline{u_r u_z} = \overline{u_x u_z}\,\cos\theta + \overline{u_y u_z}\,\sin\theta, \tag{6.2}$$

where $\overline{u_x u_z}$ and $\overline{u_y u_z}$ are the measured cross-correlations. Figure 15 shows that the pattern of $-\rho\,\overline{u_r u_z}$, normalized by ρu_B^2, is very similar for the 'low' and 'high' bulk Reynolds numbers. It also shows that, in the top part of the cross-section, the pattern of the Reynolds shear-stress is similar to that in single-phase flow (without particles), with a local maximum close to the wall. In the bottom part, close to the wall, according to the explanation given above on the 'blockage' effect, the Reynolds shear stress is decreased. However, above the particle-forcing region ($-0.01\ \mathrm{m} \lessapprox y \lessapprox 0$), the Reynolds shear stress is significantly increased, and it is larger than, for example, the Reynolds shear stress close to the wall in the top of the cross-section. This increase in the Reynolds shear stress can be explained by the 'direct' effects of the particle-forcing. Since the particle Reynolds number, Re_p, in our experiments is quite high, a wake can develop downstream of the particles, which can increase the turbulence in the particle region.

With the measured patterns of the Reynolds shear stress and the mean axial velocity, we can investigate the effect of the particle-forcing on the production of TKE and the turbulence velocity fluctuations in the cross-section.

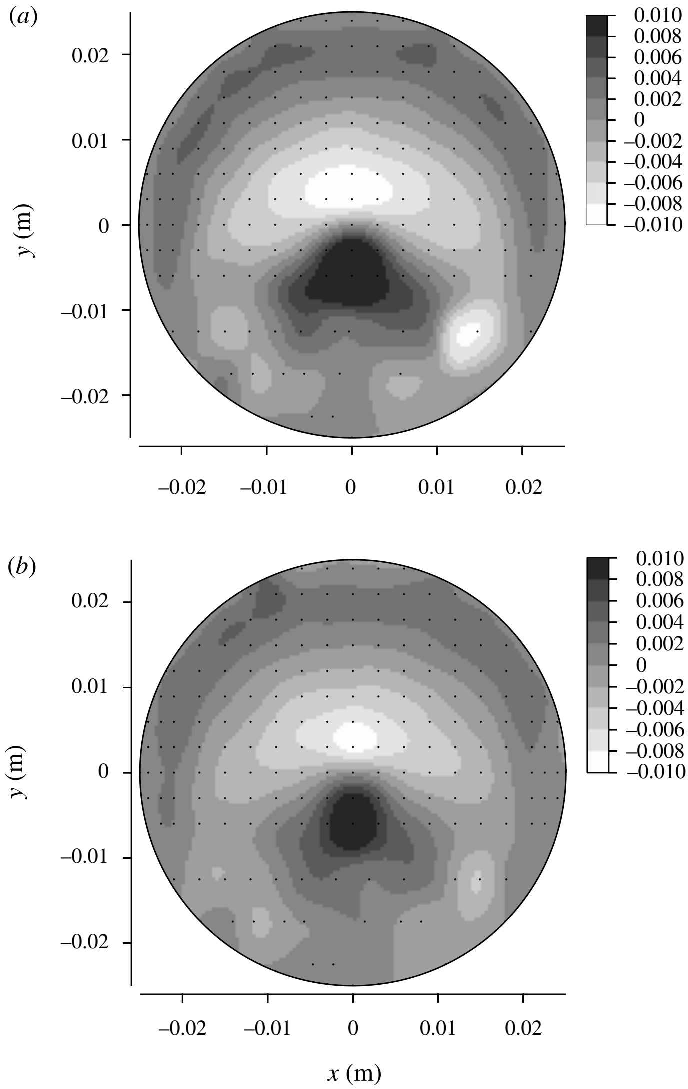

FIGURE 15. Contours of the cross-correlation $\overline{u_r u_z} = -\tau_{rz}/\rho$, normalized with the bulk velocity squared, u_B^2, for the 'low' (*a*) and 'high' (*b*) bulk Reynolds numbers.

6.3. *Turbulence kinetic energy*

The changes promoted by the particle-forcing in the axial momentum balance lead to changes in the production of turbulence from the mean flow. The production of TKE, $\mathscr{P}_k$, in Cartesian coordinates is given by

$$\mathscr{P}_k = -\overline{u_x u_z}\frac{\partial U_z}{\partial x} - \overline{u_y u_z}\frac{\partial U_z}{\partial y} - \overline{u_x u_x}\frac{\partial U_x}{\partial x} - \overline{u_y u_y}\frac{\partial U_y}{\partial y} - \overline{u_x u_y}\left(\frac{\partial U_x}{\partial y} + \frac{\partial U_y}{\partial x}\right). \quad (6.3)$$

The production of TKE is shown in figure 16. It is computed using the measured Reynolds stresses and mean velocity gradients in the Cartesian coordinate system. In the computation, we assumed that the fifth and sixth terms of (6.3) are negligible, when compared with the third and fourth terms. We show in the Appendix that this

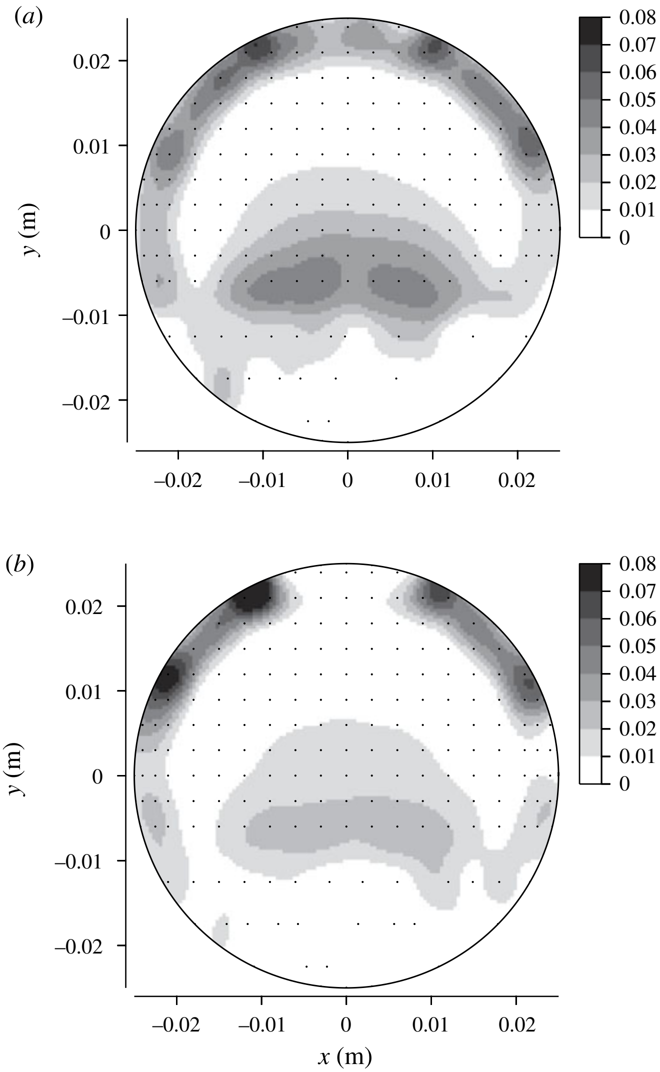

FIGURE 16. Contours of the production of TKE, $\mathscr{P}_k$, normalized by u_B^3/D, for the 'low' (*a*) and 'high' (*b*) bulk Reynolds numbers. We note that, for the 'high' bulk Reynolds number, the small production of TKE in the top of the cross-section (for $-0.01 \lessapprox x \lessapprox 0.01$ m and $0.02 \lessapprox y \leqslant 0.025$ m) is probably a measurement error and a consequence of the determination of the velocity gradients in a Cartesian coordinate system close to the wall.

assumption is likely to be correct, since $\overline{u_x u_y}$ predicted by a simple eddy-viscosity model is an order of magnitude smaller than $\overline{u_x u_x}$ and $\overline{u_y u_y}$. This assumption was necessary, since $\overline{u_x u_y}$ cannot be measured with our LDA system. Note also that the spatial resolution in the cross-section is limited. Therefore, the calculation of the velocity gradients close to the wall is imprecise, and the contours of the production of TKE only provide a qualitative picture of the actual values close to the wall.

In figure 16, the low production of TKE in the bottom part of the cross-section close to the wall is explained by the decrease of the Reynolds shear-stress and the mean axial velocity gradients due to the 'blockage' effect. The large production of

TKE in the top part of the cross-section close to the wall results from shear, similarly to single-phase turbulent pipe flows (without particles). The high production of TKE around the fixed particles is due to the non-negligible mean axial velocity gradient and the large Reynolds shear stress, which is probably caused by 'direct' effects in the particle region.

It has been verified in the calculation of $\mathscr{P}_k$ that the secondary flow has only a small contribution. This can be understood by considering the terms of (6.3). Globally, $\overline{u_x u_z}$, $\overline{u_y u_z}$, $\overline{u_x u_x}$ and $\overline{u_y u_y}$ are all of the same order of magnitude, and scale as u_∇^2. Consequently, the ratio of the third and fourth terms with respect to the first and second terms is globally the ratio of the secondary flow velocity to the mean axial velocity. Except very close to the wall, this ratio is roughly the ratio of the secondary flow velocity to the bulk velocity, i.e. in the order of a few percent. Hence, the production of TKE is mostly determined by the first and second terms in (6.3).

In figure 17, we show the TKE. In single-phase turbulent pipe flow (without particles), the pattern of the TKE resembles that of the production of TKE. It is also the case in the particle-driven secondary flow experiments: the pattern of TKE shows a local maximum close to the wall in the top part of the cross-section, which is not occurring in the bottom part, due to the 'blockage' effect, and a large value in and above the particle region, which can be due to 'direct' particle effects.

6.4. *Reynolds stresses in the cross-section*

As shown in § 2, the secondary flow results from the divergence of the Reynolds stresses in the cross-section and the mean pressure gradient in the cross-section. The pressure field has not been measured in the experiments; however, it is a reactive force to the irrotational part of $\boldsymbol{\nabla} \cdot \tilde{\boldsymbol{\tau}}$. Therefore, it should be possible to infer the direction of secondary flow from the gradients of the Reynolds stresses in the cross-section.

In cylindrical coordinates, the divergence of the Reynolds stress tensor in the cross-section, in the $\boldsymbol{e}_r$ and $\boldsymbol{e}_\theta$ directions, is given, respectively, by

$$(\boldsymbol{\nabla} \cdot \tilde{\boldsymbol{\tau}})_r = \frac{\partial \tau_{rr}}{\partial r} + \frac{1}{r}\frac{\partial \tau_{r\theta}}{\partial \theta} + \frac{\tau_{rr} - \tau_{\theta\theta}}{r}, \tag{6.4}$$

and

$$(\boldsymbol{\nabla} \cdot \tilde{\boldsymbol{\tau}})_\theta = \frac{1}{r}\frac{\partial \tau_{\theta\theta}}{\partial \theta} + \frac{\partial \tau_{r\theta}}{\partial r} + \frac{2\tau_{r\theta}}{r}, \tag{6.5}$$

where

$$\tau_{\theta\theta} = -\rho\, \overline{u_\theta u_\theta}; \quad \tau_{rr} = -\rho\, \overline{u_r u_r}; \quad \tau_{r\theta} = -\rho\, \overline{u_r u_\theta}. \tag{6.6}$$

The contours of the radial Reynolds stress, τ_{rr}, and of the circumferential Reynolds stress, $\tau_{\theta\theta}$, are shown in figure 18 for the 'low' bulk Reynolds number. Those for the 'high' bulk Reynolds number are shown in figure 19. The normal Reynolds stresses τ_{rr} and $\tau_{\theta\theta}$ are obtained from the measured normal Reynolds stresses τ_{xx} and τ_{yy}, with the assumption that the Cartesian-coordinates Reynolds shear stress in the cross-section, τ_{xy}, is negligible compared with τ_{xx} and τ_{yy}. Justification for the assumption of negligible τ_{xy} is given in the Appendix.

The Reynolds stresses in the cross-section are generated by redistribution of the axial turbulence into the cross-sectional directions. The changes promoted by the particle-forcing on the axial Reynolds stress are large, consequently small changes in the redistribution mechanism due to the particle-forcing (Li *et al.* 2001) are likely to play a minor role on the patterns of the Reynolds stresses in the cross-section, which,

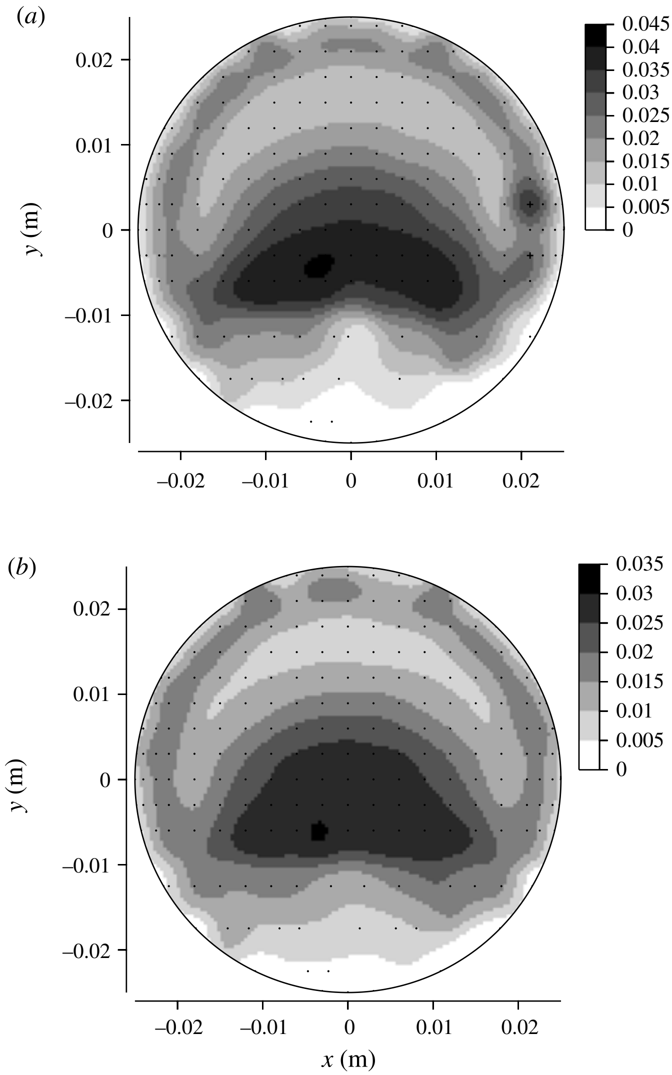

FIGURE 17. Contours of the TKE normalized with the bulk velocity squared, u_B^2, for the 'low' (*a*) and 'high' (*b*) bulk Reynolds numbers. We note that, for the 'low' bulk Reynolds number, the two large values at $x \approx 0.02$ m and $y \approx \pm 0.003$ m (grid points denoted by $+$) are probably measurement errors.

therefore, are expected to be similar to the patterns of the axial Reynolds stress. Hence, the patterns of the Reynolds stresses in the cross-section are expected to be similar to the patterns of the TKE. From figures 17, 18 and 19 we can see that, indeed, this is the case. For example, inside and close to the particle-forcing region, the Reynolds stresses in the cross-section τ_{rr} and $\tau_{\theta\theta}$ have a maximum, similar to the maximum in TKE. However, we also note differences. For example, the local maximum in τ_{rr} and $\tau_{\theta\theta}$ close to the wall, in the top part of the cross-section, is not very pronounced, especially for the 'low' bulk Reynolds number and for the radial Reynolds stress.

In the Appendix, we show that the cylindrical-coordinates Reynolds shear stress in the cross-section, $\tau_{r\theta}$, is much smaller than the cylindrical-coordinates normal

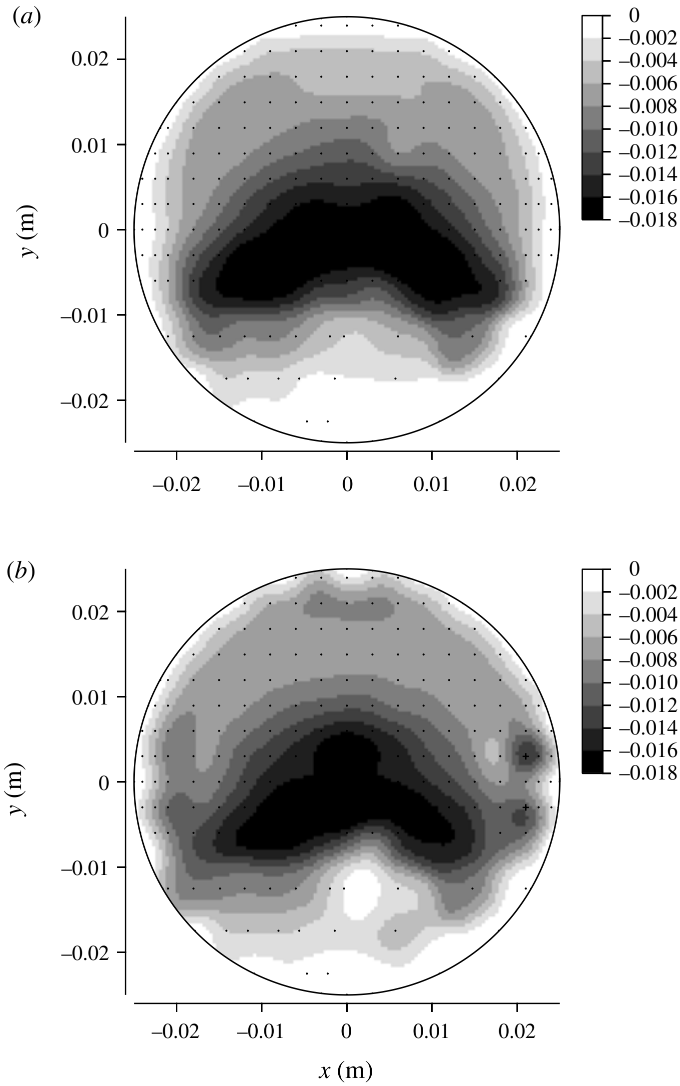

FIGURE 18. Contours of the radial Reynolds stress $-\rho\overline{u_r u_r}$ (*a*) and of the circumferential Reynolds stress $-\rho\overline{u_\theta u_\theta}$ (*b*), normalized with ρu_B^2, for the 'low' bulk Reynolds number. We note that the two large peaks at $x \approx 0.02$ m and $y \approx \pm 0.003$ m in the contours of the circumferential Reynolds stress (grid points denoted by $+$) are probably measurement errors.

Reynolds stresses in the cross-section, τ_{rr} and $\tau_{\theta\theta}$, and that the patterns of $\tau_{r\theta}$ do not show strong gradients. Apparently, the particle-forcing does not have a large impact on $\tau_{r\theta}$, since in single-phase turbulent pipe flow (without particles) $\tau_{r\theta}$ is exactly equal to zero. We note that this is different from square pipes, where the gradients of the Reynolds shear-stress in the cross-section play a major role in the determination of the secondary flow (Demuren & Rodi 1984). Therefore, in our experiments, the radial and circumferential components of $\boldsymbol{\nabla}\cdot\tilde{\boldsymbol{\tau}}$ are mainly determined by the Reynolds stresses τ_{rr} and $\tau_{\theta\theta}$. Furthermore, figure 20 shows that the radial component, $(\boldsymbol{\nabla}\cdot\tilde{\boldsymbol{\tau}})_r$, is mainly determined by the gradient of τ_{rr} with respect to the radial direction, since in (6.4) the term $(\tau_{\theta\theta} - \tau_{rr})/r$ represents at most $\approx$20 % of the term $\partial\tau_{rr}/\partial r$.

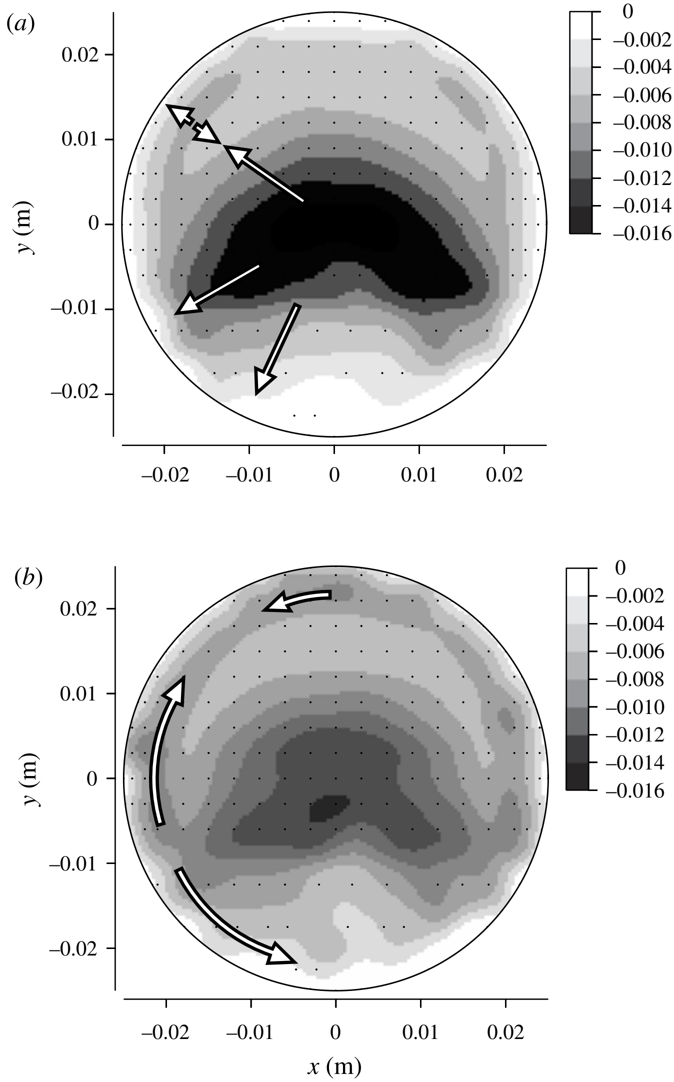

FIGURE 19. Contours of the radial Reynolds stress $-\rho\overline{u_r u_r}$ (*a*) and of the circumferential Reynolds stress $-\rho\overline{u_\theta u_\theta}$ (*b*), normalized with ρu_B^2, for the 'large' bulk Reynolds number.

Due to the symmetry with respect to the y-axis, there exist at least two secondary flow cells. Due to this symmetry, we only need to consider in the left-hand side of the cross-section (i) the gradient of τ_{rr} with respect to r and (ii) the gradient of $\tau_{\theta\theta}$ with respect to θ, to predict the secondary flow direction. This reasoning needs to be made for only one bulk Reynolds number, since the patterns of the Reynolds stresses τ_{rr} and $\tau_{\theta\theta}$ are very similar for the two bulk Reynolds numbers.

Figures 18 and 19 show that, close to the wall, the gradient of the circumferential Reynolds stress with respect to θ pushes the flow (i) in the $\boldsymbol{e}_\theta$ direction for θ between $\pi/2$ and $\approx 3\pi/4$, and strongly in that direction for θ between $\approx 7\pi/6$ and $3\pi/2$; and (ii) in the $-\boldsymbol{e}_\theta$ direction for θ between $\approx 3\pi/4$ and $\approx 7\pi/6$ (see the arrows in figure 19). The comparison with the secondary flow fields in figure 10 shows that, indeed, we

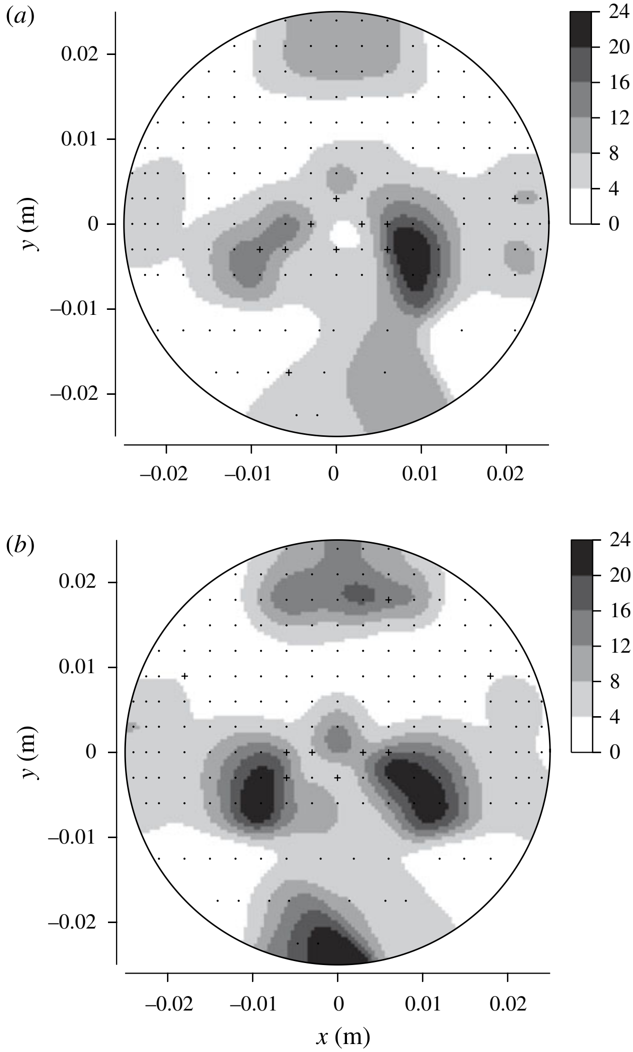

FIGURE 20. Contours of the term $(\tau_{\theta\theta} - \tau_{rr})/r$ compared with the term $\partial\tau_{rr}/\partial r$ (in % and in absolute value), in the driving force in the radial direction, $(\boldsymbol{\nabla} \cdot \tilde{\boldsymbol{\tau}})_r$, for the 'low' (*a*) and 'high' (*b*) bulk Reynolds numbers. Note that the values measured at the grid points denoted by $+$ are not accounted for in the contours, since these values are abnormally high (mainly due to the division by r close to $r = 0$).

have a strong secondary flow velocity close to the wall for θ between $\approx 7\pi/6$ and $3\pi/2$, and in the same direction as $(\boldsymbol{\nabla} \cdot \tilde{\boldsymbol{\tau}})_\theta$ between these angles. The elongated cell of small amplitude in the top part of the cross-section flows in the same direction as that of the driving force in the circumferential direction, $(\boldsymbol{\nabla} \cdot \tilde{\boldsymbol{\tau}})_\theta$, for θ between $3\pi/4$ and $\approx 7\pi/6$, but in the opposite direction for θ between $\pi/2$ and $3\pi/4$.

Figures 18 and 19 also show that the gradient of the radial Reynolds stress with respect to the radial direction pushes the flow mostly in the $\boldsymbol{e}_r$ direction, except in a small region in the top of the cross-section, between the local minimum close to the wall and the local maximum in τ_{rr}, where the flow is weakly pushed in the

$-\boldsymbol{e}_r$ direction (see the arrows in figure 19). The driving force in the radial direction, $(\nabla \cdot \tilde{\boldsymbol{\tau}})_r$, is strongest close to the wall at $\theta \approx 7\pi/6$, where it is in the $\boldsymbol{e}_r$ direction. The secondary flow velocity fields in figure 10 show that, indeed, close to the wall at $\theta \approx 7\pi/6$, the two cells in the left-hand side flow in the $\boldsymbol{e}_r$ direction.

The secondary flow results from the integral of $\nabla \cdot \tilde{\boldsymbol{\tau}}$ in the cross-section. For the large cell in the left-hand side of the bottom part of the cross-section, the integration of $(\nabla \cdot \tilde{\boldsymbol{\tau}})_\theta$ at a small distance ℓ, from the wall, for θ from $\approx 7\pi/6$ to $3\pi/2$, is equal to $\tau_{\theta\theta}\,(\theta = 3\pi/2) - \tau_{\theta\theta}\,(\theta \approx 7\pi/6)$, i.e. it leads to a positive contribution in the $\boldsymbol{e}_\theta$ direction, which is also the direction of the secondary flow cell. The integration of $(\nabla \cdot \tilde{\boldsymbol{\tau}})_r$ from the centre to ℓ, at $\theta \approx 7\pi/6$, and back to the centre from that same distance ℓ, at $\theta = 3\pi/2$, is equal to $\tau_{rr}\,(\theta \approx 7\pi/6) - \tau_{rr}\,(\theta = 3\pi/2)$, and it is a negative contribution, in the opposite direction of the secondary flow cell. However, similarly to single-phase flow, close to the wall τ_{rr} is smaller in amplitude than $\tau_{\theta\theta}$, which is due to the no-flux condition through the wall for the radial velocity. This fact can also be seen by comparing the contours of τ_{rr} and $\tau_{\theta\theta}$, in figures 18 and 19. Therefore, the contribution in the circumferential direction is larger than that in the radial direction, and it imposes the direction of the secondary flow. A similar reasoning can be made for the elongated cell in the left-hand side of the top part of the cross-section, except that, in this case, the direction is mainly imposed by the radial Reynolds stress, when performing the integration of $\nabla \cdot \tilde{\boldsymbol{\tau}}$.

7. Scaling of the particle-driven secondary flow with the mean axial forcing

The occurrence of secondary flow is an inertial effect. Integrating the Reynolds-averaged Navier–Stokes equations in the cross-section between two regions, one with and one without particle-forcing, and neglecting the influence of the viscous forces, we get

$$\rho \Delta \left|\boldsymbol{V}\right|^2 \sim \Delta \tilde{\tau}, \tag{7.1}$$

where $\Delta \left|\boldsymbol{V}\right|^2$ is the difference in the secondary flow velocity squared, between the region with and the region without particle-forcing, and $\Delta \tilde{\tau}$ is the difference in the normal Reynolds stresses in the cross-section, between the same regions. The secondary flow velocity, $|\boldsymbol{V}|$, will be largest where the gradients in $\tilde{\tau}$ are strongest, and far from large gradients the secondary flow velocity will be small; therefore, $\Delta \left|\boldsymbol{V}\right|^2$ will be roughly equal to the square of the maximum secondary flow velocity itself. Consequently, we have

$$\rho \left|\boldsymbol{V}\right|^2 \sim \Delta \tilde{\tau}. \tag{7.2}$$

Hence, the prediction of the maximum secondary flow velocity requires the prediction of the Reynolds stresses in the cross-section. In the region far from the particle-forcing, the Reynolds stresses in the cross-section globally scale with the friction velocity squared, u_∇^2, based on the mean pressure-gradient in the axial direction. Hence, we have

$$\tilde{\tau}_N \sim \rho u_\nabla^2, \tag{7.3}$$

where $\tilde{\tau}_N$ are the Reynolds stresses in the cross-section far from the particle-forcing region.

Because of the 'blockage' effect, the Reynolds stresses in the cross-section close to the particle-forcing region scale globally with the effective pressure gradient, which is the sum of the mean axial pressure gradient and the mean axial forcing. Hence, for the

Reynolds stresses in the cross-section close to the particle-forcing region, $\tilde{\tau}_F$, we have

$$\tilde{\tau}_F \sim \rho u_\nabla^2 + \frac{\bar{\mathfrak{F}}_z}{4/D}, \tag{7.4}$$

with $\bar{\mathfrak{F}}_z < 0$.

From the difference between τ_N and τ_F, we obtain the scaling law for the maximum secondary flow velocity, given by

$$\rho\,|\boldsymbol{V}|^2 \sim \frac{|\bar{\mathfrak{F}}_z|}{4/D}. \tag{7.5}$$

We note here that the 'direct' effects promoted by the particle-forcing will probably also scale with the mean axial forcing, giving the same result as in (7.5).

To derive a scaling, we assume that, at each fixed particle, the mean axial velocity is equal to the bulk velocity u_B. Then, the forcing, $|\bar{\mathfrak{F}}_z|$, can be written as

$$|\bar{\mathfrak{F}}_z| \sim N_p\,\frac{1}{2}\rho u_B^2\,\frac{\pi D_p^2}{4}\,C_D, \tag{7.6}$$

where N_p is the number particle density ($N_p \approx 1.5 \times 10^6$ particles per cubic metre, in our experiments) and C_D is the drag coefficient, based here on the bulk velocity, u_B. Replacing (7.6) in (7.5), we obtain the scaling

$$\left(\frac{|\boldsymbol{V}|}{u_B}\right)^2 \sim \frac{\pi}{32}\,N_p\,D_p^2\,D\,C_D. \tag{7.7}$$

This scaling indicates that the ratio between the secondary flow velocity and the bulk velocity is proportional to the number particle density and that it is constant at very high Reynolds numbers, since in that case the drag coefficient would be a constant. Unfortunately, it was not possible to verify this, because of the limited range in the bulk Reynolds number and the constant number of fixed particles in our experimental set-up.

In the conditions of our experiments, the particle Reynolds numbers are equal to 110 and 217, at the 'low' and 'high' bulk Reynolds numbers, respectively. For such particle Reynolds numbers, C_D can be expressed by the standard drag relation:

$$C_D = \frac{24}{Re_p}\left(1 + 0.15 Re_p^{0.687}\right). \tag{7.8}$$

Consequently, the scaling law of the secondary flow velocity in our experimental set-up is

$$\left(\frac{|\boldsymbol{V}|}{u_B}\right)^2 \sim \frac{3\pi}{4}\,N_p\,D_p\,D^2\,\frac{1}{Re_B}\left(1 + 0.15\left(D_p/D\right)^{0.687} Re_B^{0.687}\right). \tag{7.9}$$

Our experiments show a good scaling of the secondary flow with the bulk Reynolds number; see figure 10. An increase of the bulk Reynolds number by a factor 1.98 led to an increase of the secondary flow velocity by a factor 1.51. The scaling law in (7.9) predicts an increase of 1.72 in the secondary flow velocity, which is reasonably close to our experimental value of 1.51. Due to the low bulk Reynolds numbers in the experiments, it is possible that viscous effects cannot be neglected, which could be one explanation for the small overestimation. More measurements at larger Reynolds numbers would be useful: to check whether this is related, or not, to a Reynolds number effect, and also to verify the scaling (since the results above are based on only two Reynolds numbers). However, such measurements are not feasible in our set-up, because the lines on which the particles are fixed start to vibrate at larger Reynolds numbers.

We also note that a proportionality constant of 1 in (7.9) (i.e. $\sim$ replaced by $=$) would lead to a secondary flow velocity of 8.9 % and 7.6 % of the bulk velocity, for the 'low' and 'high' bulk Reynolds numbers, respectively. These values are close to the measured values of the maximum secondary flow velocity; see figure 11. This indicates that the approximations made in (7.1)–(7.9) are reasonable and that the proportionality constant is effectively close to 1 in (7.9).

8. Conclusion

In the literature, it is known that secondary flow occurs in single-phase turbulent flows in (i) pipes of non-circular cross-section and/or (ii) in pipes with non-uniform boundary conditions, and that it is driven by the anisotropy in the Reynolds stresses in the cross-section. In this work, we show that a non-uniform internal forcing, for example the forcing on the flow by particles distributed non-uniformly in the cross-section, can also promote a secondary flow. Indeed, in a turbulent pipe flow, particle-forcing can promote changes in the turbulence, which, in the case of non-uniformly distributed particles, results in an anisotropy in the Reynolds stresses in the cross-section, which promotes secondary flow. Here, we provide experimental support for the occurrence of particle-driven secondary flow in a fully developed turbulent pipe flow of circular cross-section.

Laser Doppler anemometry experiments were performed to measure the secondary flow velocity field promoted by a non-uniform distribution of particles. A well-defined situation, in which the particles are kept at fixed positions in the pipe, was chosen, in order to study the relation between the occurrence of secondary flow and the turbulence modification. Using this configuration, other mechanisms that could promote secondary flow (for example, a forcing in the cross-section) or obscure the relation between secondary flow and turbulence modification (for example, particle dispersion) are avoided. Our measurements show the occurrence of a particle-driven secondary flow, which consists of four cells for our particle distribution, with the required symmetry with respect to the symmetry axis, and which is of relatively large magnitude (up to 9 % of the bulk velocity).

Particle-forcing in the axial direction can promote a turbulence modification due to (i) 'direct' effects, which are associated with the local distortion of the flow field around the particles; and (ii) 'indirect' effects, which are associated with the changes the particles promote in the balance of momentum and in the global turbulence dynamics. The measurements showed the occurrence of both the 'indirect' and 'direct' turbulence modification. Due to the balance of axial momentum, the drag force has a 'blockage' effect, which reduces the mean axial velocity and the Reynolds shear stress in the part of the pipe where the particles are located, which, in turn, reduces the production of turbulence and the turbulence itself. However, in the proximity of the particles, 'direct' or 'wake' effects are observed, which results in an increase of the turbulence around the particles. 'Wake' effects could be observed due to the large particle Reynolds numbers in the experiments.

The measurements showed that the divergence of the Reynolds stress tensor in the cross-section can be used to predict the direction of the secondary flow. It appears that the gradients of the radial and circumferential Reynolds stresses, in the radial and circumferential directions, respectively, are the dominant terms in the divergence of the Reynolds stress tensor in the cross-section; and that they determine the secondary flow pattern.

The experiments show a good scaling of the secondary flow velocity with the bulk Reynolds number. Based on the 'blockage' mechanism, a scaling law has been proposed, in which the secondary flow velocity scales with the root of the mean particle-forcing (which is a function of the bulk Reynolds number). This scaling law reproduces reasonably well the scaling observed in the experiments. Furthermore, the scaling law also predicts correctly the magnitude of the secondary flow. However, due to the limitations in our experimental set-up, we did not perform a full validation for a larger range of Reynolds numbers.

Acknowledgement

Financial support was provided by STW for the research project 'Liquid loading in inclined pipes for gas production and transport'.

Appendix

In this appendix, we show that neglecting the Reynolds shear stress in the cross-section is justified.

The cross-correlation $\overline{u_x u_y}$ cannot be measured with our LDA set-up. However, $\tau_{xy} = -\rho\overline{u_x u_y}$ intervenes in the calculation of the cylindrical-coordinates components of the Reynolds stress tensor in the cross-section (τ_{rr}, $\tau_{\theta\theta}$ and $\tau_{r\theta}$) from its Cartesian-coordinates components (τ_{xx}, τ_{yy} and τ_{xy}). Since τ_{xy} cannot be measured, only the measured normal Reynolds stresses τ_{xx} and τ_{yy}, are taken into account in our calculations. Here, we compute τ_{xy} from an eddy-viscosity model, using the measured LDA data, and show that neglecting τ_{xy} is justified.

The grid resolution in our experiments is too small to compute accurately τ_{xy} from a Reynolds stress model. Furthermore, a Reynolds stress model is complicated by the low Reynolds numbers at which the experiments are performed, and at which local equilibrium cannot be assumed. Therefore, we use the simple explicit eddy-viscosity model, which usually performs quite well for the Reynolds shear stress in a pipe:

$$\overline{u_x u_y} = -\nu_t \left(\frac{\partial U_x}{\partial y} + \frac{\partial U_y}{\partial x} \right), \tag{A 1}$$

where ν_t is the eddy viscosity, which could be computed from, for example, a mixing-length model. However, due to the low Reynolds number, an accurate model for the eddy viscosity cannot be easily specified; instead, we calculate its value using the above expression for the axial Reynolds shear stresses τ_{xz} and τ_{yz}, which are measured. Both τ_{xz} and τ_{yz} gave a similar value of the eddy viscosity. It is checked that this approach gives also a good estimate of τ_{xy} in the DNS of Belt (2007), except very close to a zero gradient in the mean axial velocity, which does not exactly correspond to a zero axial Reynolds shear stress (due to convection by secondary flow), and, therefore, gives abnormally high values of the eddy viscosity. However, in our experiments, the grid resolution is too low to obtain exactly a zero gradient in the mean axial velocity, and the approach does not give rise to erroneous values of the eddy viscosity.

The predicted Cartesian-coordinates Reynolds shear stress in the cross-section, τ_{xy}, is shown in figure 21. The magnitude of τ_{xy} is, indeed, much smaller than that of τ_{xx}

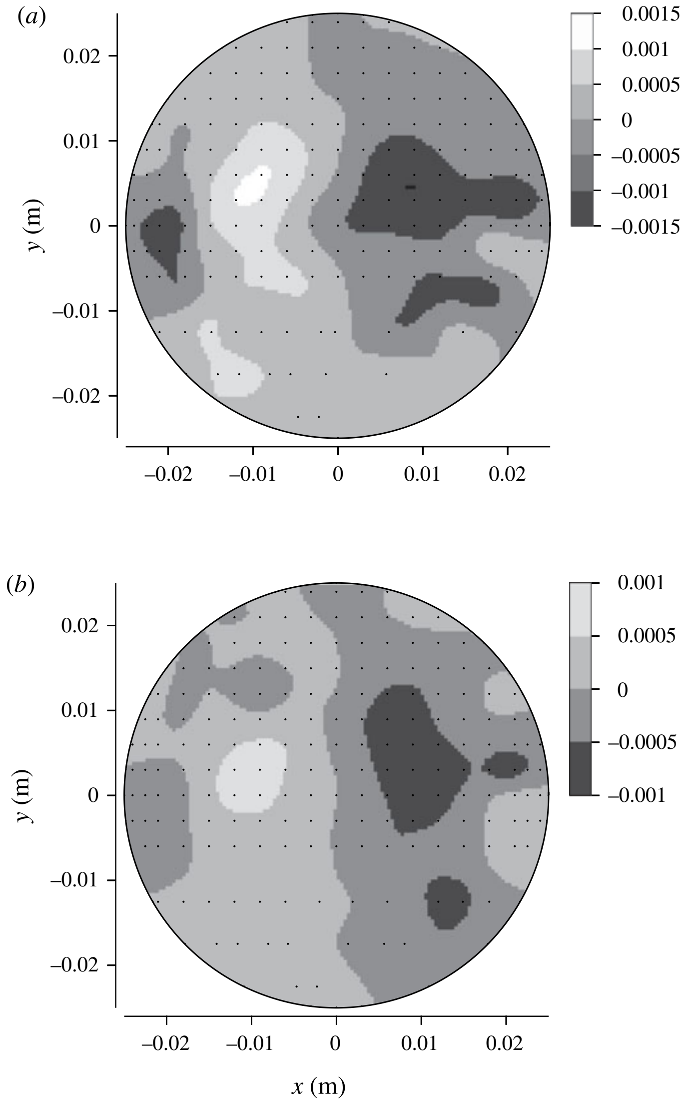

FIGURE 21. Contours of the predicted Cartesian-coordinates Reynolds shear-stress in the cross-section, τ_{xy}, normalized with ρu_B^2, for the 'low' (a) and 'high' (b) bulk Reynolds numbers.

and τ_{yy}, meaning that the Reynolds stresses, τ_{rr} and $\tau_{\theta\theta}$ are correctly predicted from τ_{xx} and τ_{yy} when τ_{xy} is neglected.

The cylindrical-coordinates Reynolds shear stress in the cross-section, $\tau_{r\theta} = -\rho\overline{u_r u_\theta}$, and its gradients with respect to r and θ appear in the divergence of the Reynolds stress tensor in the cross-section ((6.4) and (6.5)). However, since $\tau_{r\theta}$ is strongly related to τ_{xy}, we do not take into account $\tau_{r\theta}$ and its gradients in the evaluation of $(\boldsymbol{\nabla}\cdot\tilde{\boldsymbol{\tau}})_r$ and $(\boldsymbol{\nabla}\cdot\tilde{\boldsymbol{\tau}})_\theta$.

Indeed, the cross-correlation $\overline{u_r u_\theta}$ is given by

$$\overline{u_r u_\theta} = \overline{u_x u_y}\,(2\cos^2\theta - 1) + \cos\theta\sin\theta(\overline{u_y u_y} - \overline{u_x u_x}). \tag{A 2}$$

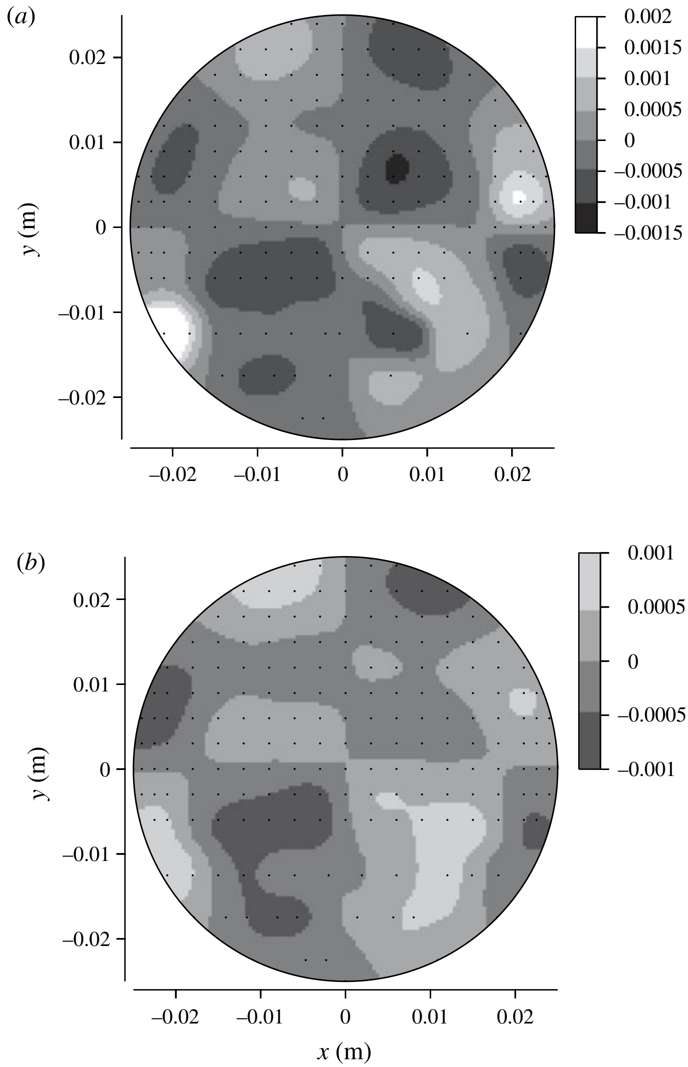

FIGURE 22. Contours of the part of the cylindrical-coordinates Reynolds shear-stress in the cross-section, $\tau_{r\theta}$, associated with the difference between τ_{yy} and τ_{xx}, normalized with ρu_B^2, for the 'low' (*a*) and 'high' (*b*) bulk Reynolds numbers.

Therefore, $\tau_{r\theta}$ has two parts: (i) a part associated with τ_{xy} (the first term in (A 2)); and (ii) a part associated with the difference between τ_{yy} and τ_{xx} (the second term in (A 2)). The second part can be obtained from the measured values of τ_{xx} and τ_{yy}, and is shown in figure 22; its magnitude is much smaller than the magnitude of τ_{xx} and τ_{yy}, and, globally, is of the same order of the magnitude of the first part of $\tau_{r\theta}$ (obtained from the predicted values τ_{xy}).

From figures 21 and 22, is clear that $\tau_{r\theta}$ is an order of magnitude smaller than the radial and circumferential Reynolds stresses, and that it does not have strong gradients. This confirms that the effect of $\tau_{r\theta}$ on the divergence of the Reynolds stress tensor in the cross-section is small. It is checked that in the DNS of Belt (2007) $\tau_{r\theta}$ was also very small, and much smaller than τ_{rr} and $\tau_{\theta\theta}$. Apparently, the particle-forcing does not have an impact on $\tau_{r\theta}$, since in single-phase turbulent pipe flow (without particles) $\tau_{r\theta}$ is exactly equal to zero.

From the results presented here, is clear that the influence of τ_{xy} and $\tau_{r\theta}$ on the secondary flow is small and that, indeed, is justified to neglect the Reynolds shear stress in the cross-section.

REFERENCES

ABSIL, L. H. J. 1995 Analysis of the laser Doppler measurement technique for application in turbulent flows. PhD thesis, Delft University of Technology.

BELT, R. J. 2007 On the liquid film in inclined annular flow. PhD thesis, Delft University of Technology.

BENEDICT, L. H., NOBACH, H. & TROPEA, C. 2000 Estimation of turbulent velocity spectra from laser Doppler data. *Meas. Sci. Technol.* **11** (8), 1089–1104.

BOIVIN, M., SIMONIN, O. & SQUIRES, K. D. 1998 Direct numerical simulation of turbulence modulation by particles in isotropic turbulence. *J. Fluid Mech.* **375**, 235–263.

BRUNDRETT, E. & BAINES, W. D. 1964 The production and diffusion of vorticity in duct flow. *J. Fluid Mech.* **19** (3), 375–394.

DAALMANS, A. C. L. M. 2005 Laser Doppler anemometry measurements of particle-driven secondary flow in turbulent horizontal pipe flow. MSc thesis, Delft University of Technology.

DARLING, R. S. & MCMANUS, H. N. 1968 Flow patterns in circular ducts with circumferential variation of roughness: a two-phase flow analog. *Dev. in Mech.: Proc. 11th Midwestern Mech. Conf.* **5**, 153–163.

DEMUREN, A. O. & RODI, W. 1984 Calculation of turbulence-driven secondary motion in non-circular ducts. *J. Fluid Mech.* **140**, 189–222.

DYKHNO, L. A., WILLIAMS, L. R. & HANRATTY, T. J. 1994 Maps of mean gas velocity for stratified flows with and without atomization. *Intl J. Multiphase Flow* **20** (4), 691–702.

EGGELS, J. G. M., UNGER, F., WEISS, M. H., WESTERWEEL, J., ADRIAN, R. J., FRIEDRICH, R. & NIEUWSTADT, F. T. M. 1994 Fully developed turbulent pipe flow: a comparison between direct numerical simulation and experiment. *J. Fluid Mech.* **268**, 175–209.

FLORES, A. G., CROWE, K. E. & GRIFFITH, P. 1995 Gas-phase secondary flow in horizontal, stratified and annular two-phase flow. *Intl J. Multiphase Flow* **21** (2), 207–221.

HALLEZ, Y. & MAGNAUDET, J. 2009 Turbulence-induced secondary motion in a buoyancy-driven flow in a circular pipe. *Phys. Fluids* **21**, 081704.

HARTEVELD, W. K. 2005 Bubble columns: structures or stability? PhD thesis, Delft University of Technology.

HINZE, J. O. 1973 Experimental investigation on secondary currents in the turbulent flow through a straight conduit. *Appl. Sci. Res.* **28**, 453–465.

HUBER, N. & SOMMERFELD, M. 1998 Modelling and numerical calculation of dilute-phase pneumatic conveying in pipe systems. *Powder Technol.* **99**, 90–101.

LAUNDER, B. E. & YING, W. M. 1972 Secondary flows in ducts of square cross-section. *J. Fluid Mech.* **54** (2), 289–295.

LI, Y., MCLAUGHLIN, J. B., KONTOMARIS, K. & PORTELA, L. 2001 Numerical simulation of particle-laden turbulent channel flow. *Phys. Fluids* **13** (10), 2957–2967.

LINÉ, A., MASBERNAT, L. & SOUALMIA, A. 1994 Interfacial interactions and secondary flows in stratified two-phase flow. *Chem. Engng Commun.* **141–142**, 303–329.

NAGATA, K., HUNT, J. C. R., SAKAI, Y. & WONG, H. 2011 Distorted turbulence and secondary flow near right-angled plates. *J. Fluid Mech.* **668**, 446–479.

NOBACH, H. 2002 Local time estimation for the slotted correlation function of randomly sampled LDA data. *Exp. Fluids* **32** (3), 337–345.

NORDSVEEN, M. 2001 Wave- and turbulence-induced secondary currents in the liquid phase in stratified duct flow. *Intl J. Multiphase Flow* **27** (9), 1555–1577.

PORTELA, L. M., COTA, P. & OLIEMANS, R. V. A. 2002 Numerical study of the near-wall behaviour of particles in turbulent pipe flows. *Powder Technol.* **125** (2–3), 149–157.

SPEZIALE, C. G. 1982 On turbulent secondary flows in pipes of noncircular cross-section. *Intl J. Engng Sci.* **20** (7), 863–872.

SQUIRES, K. D. & EATON, J. K. 1990 Particle response and turbulence modification in isotropic turbulence. *Phys. Fluids* A **2**, 1191–1203.

TOWNSEND, A. A. 1976 *The Structure of Turbulent Shear Flow*. Cambridge University Press.

TUMMERS, M. J. 1999 Investigation of a turbulent wake in an adverse pressure-gradient using laser Doppler anemometry. PhD thesis, Delft University of Technology.

VAN MAANEN, H. R. E. 1999 Retrieval of turbulence and turbulence properties from randomly sampled laser-Doppler anemometry data with noise. PhD thesis, Delft University of Technology.

VAN'T WESTENDE, J. M. C., BELT, R. J., PORTELA, L. M., MUDDE, R. F. & OLIEMANS, R. V. A. 2007 Effect of secondary flow on droplet distribution and deposition in horizontal annular pipe flow. *Intl J. Multiphase Flow* **33** (1), 67–85.